Unraveling the host-selective toxic interaction of cassiicolin with lipid membranes and its cytotoxicity

Key words: Lipid membranes, host-selective toxin, cassiicolin, *Corynespora cassiicola*, HS-AFM

Running title: Host-selective toxic interaction of cassiicolin with lipids

Kien Xuan Ngo[1#*], Nguyen Bao Quoc[2#*], Phuong Doan N. Nguyen[1,2], Hirotoshi Furusho[1], Makoto Miyata[3], Tomomi Shimonaka[3], Nguyen Ngoc Bao Chau[4], Nguyen Phuong Vinh[5], Nguyen Anh Nghia[5], Tareg Omer Mohammed[1], Takehiko Ichikawa[1], Noriyuki Kodera[1], Hiroki Konno[1], Takeshi Fukuma[1], Toshio Ando[1]

Affiliations

[1]Nano Life Science Institute (WPI-NanoLSI), Kanazawa University, Kakuma-machi, Kanazawa, Japan.

[2]Research Institute for Biotechnology and Environment, Nong Lam University, Ho Chi Minh City, Vietnam.

[3]Department of Biology, Graduate School of Science, Osaka City University, Osaka, Japan.

[4]Faculty of Biotechnology, Ho Chi Minh City Open University, Ho Chi Minh City, Vietnam.

[5]Rubber Research Institute of Vietnam, Ho Chi Minh City, Vietnam.
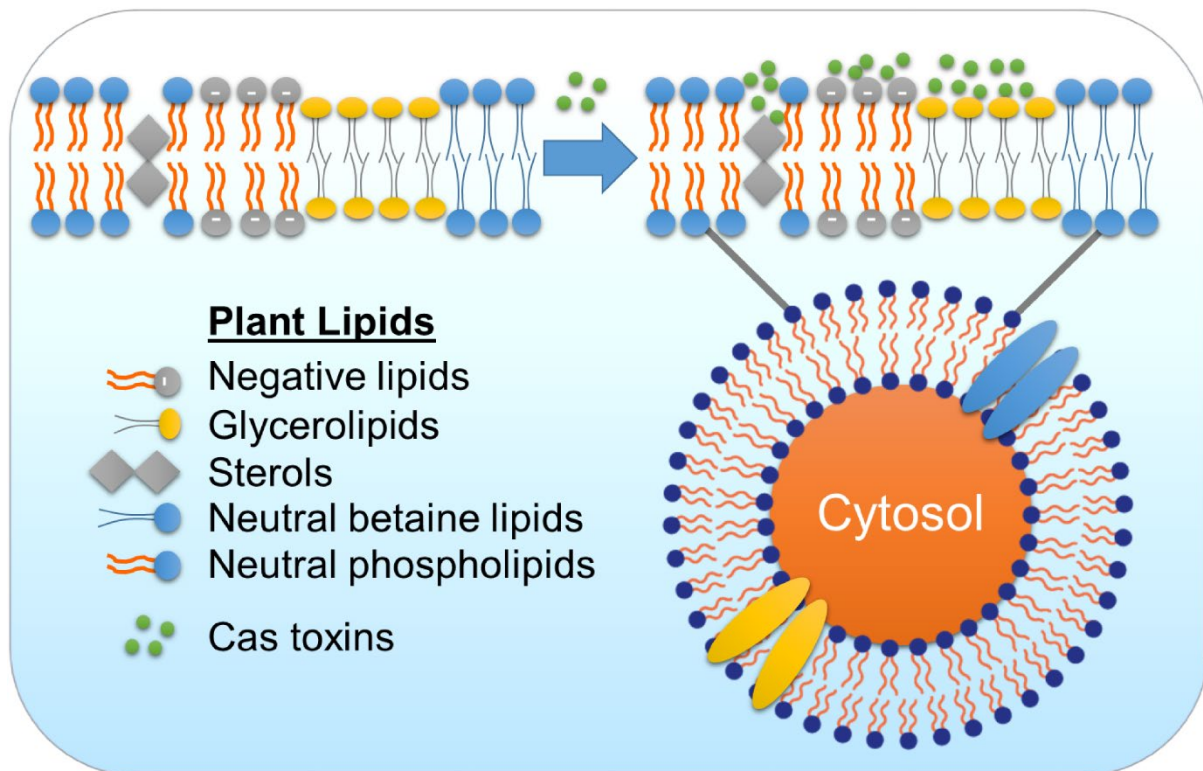
Corresponding authors (*)

Kien Xuan Ngo (ngoxuankien@staff.kanazawa-u.ac.jp)

Nguyen Bao Quoc (baoquoc@hcmuaf.edu.vn)

[#]These authors contributed equally.

Graphic abstract

Highlights

➢ Cas1 and Cas2 directly damage and cause necrosis in the leaves of the susceptible rubber clones

➢ Specific cytoplasmic membranes of plant cells are highly vulnerable to the cytotoxicity of selective Cas toxin

➢ Negative phospholipids (PA), glycerolipids (MGDG, DGDG), and specific sterols (stigmasterol, sitosterol) in cytoplasmic membranes are highly susceptible to Cas1 and/or Cas2

Abstract

Corynespora cassiicola is the pathogen that causes Corynespora leaf fall (CLF) disease. Cassiicolin (Cas), a toxin produced by *C. cassiicola*, is responsible for CLF disease in rubber trees (*Hevea brasiliensis*). Currently, the molecular mechanism of the cytotoxicity of Cas and its host selectivity have not been fully elucidated. To gain insight into these issues, we analyzed the binding of Cas1 and Cas2 to membranes consisting of different plant lipids and their membrane-disruption activities. Our real-time observations with high-speed atomic force microscopy (HS-AFM) and confocal microscopy reveal that the binding and disruption activities of Cas1 and Cas2 are strongly dependent on the types of membrane lipids. The mixtures of DPPC with DPPA, MGDG, DGDG, and stigmasterol are more susceptible to membrane damage caused by Cas1 and Cas2 than DPPC alone or its mixtures with sitosterol, DGTS-d9, and DGTS. This difference derives from the stronger binding of the toxins to membranes with the former lipid composition. Cytotoxicity tests on rubber leaves of RRIV 1, RRIV 4, and PB 255 clones suggest that the toxins cause necrosis of rubber leaves, except for the strong resistance of PB 255 against Cas2. Cryo-SEM analyses of necrotic leaf tissues exposed to Cas1 confirm that cytoplasmic membranes are vulnerable to the toxin. Thus, the host selectivity of Cas toxin in CLF disease is attained by the lipid-dependent binding activity of Cas to the membrane, and the cytotoxicity of Cas arises from its ability to disrupt membranes.

Introduction

The necrotrophic fungus *Corynespora cassiicola* (Berk.&Curt) Wei is a causal pathogen of corynespora leaf fall (CLF) disease in rubber leaves, of which the typical symptoms are brown leaf lesions surrounded by a yellow halo and occasional blackening of the veins, which causes a symptomatic "fish-bone" appearance, resulting in massive defoliation in susceptible rubber clones [1]. *C. cassiicola* predominantly infects both young and mature leaves, and CLF disease has now become widespread in *Hevea brasiliensis* plantations, causing severe damage to the natural rubber industry. These pathogens have also been found in many other crops [2–4]. Although the first pathogenic *C. cassiicola* isolate originally from the Philippines (CCP) is described as a causal agent in CLF disease, a necrotrophic effector known as cassiicolin (Cas) toxin produced in CCP is widely accepted as the host-selective toxin (HST) interaction in rubber trees and other plants [1,5–9]. The Cas-encoding genes were found to be transiently expressed one or two days post inoculation, suggesting a role of Cas toxin in the early phase of infection [9]. Cas toxin is a small glycosylated secreted protein effector associated with secondary metabolism in *C. cassiicola* [5–7,9]. To date, six cassiicolin isoforms (Cas1 to Cas6) have been genetically identified by PCR-based detection from fungal isolates in various host plants and geographical origins [7,9]. Of note, *C. cassiicola* isolates only carry and express specific Cas genes, depending on the host specialization [7,10–13]. Some *C. cassiicola* isolates possessing no Cas gene yet causing CLF diseases may reveal other putative effectors involved

[10]. The nature of the HST interaction of Cas toxin in CLF disease remains controversial because *in silico* analysis and prediction revealed 2870 putative effectors comprising CaZymes, lipases, peptidases, and secreted proteins and enzymes associated with secondary metabolism of *C. cassiicola* [10]. However, recent studies reported that gene deletion of Cas1 in *C. cassiicola* completely suppresses fungal pathogenicity in rubber trees [1,14]. These studies suggested two important findings: (i) Cas1 is a necrotrophic effector conferring virulence to *C. cassiicola* in susceptible rubber clones; (ii) other effectors produced in *C. cassiicola* contribute to residual filtrate toxicity and virulence in senescing/wounded tissues. These putative effectors may be involved in saprotrophs rather than necrotrophs [1,14]. However, the cytotoxicity of Cas2 on rubber leaves has never been clarified before and remains unknown. Of special interest, we further examined and clarified the cytotoxicity of Cas isoforms (i.e., Cas1 and Cas2) to understand the fundamental molecular mechanisms underlying the HST interaction of Cas toxin in leaves of various rubber clones. In this context, the direct cytotoxicity of Cas1 to rubber leaves has been explored in some previous studies [5,6,15]. Notably, purified Cas1 applied on rubber leaves caused the same symptoms as *C. cassiicola* at the cellular level [5,6]. Electron microscopic analyses of necrotic leaf tissues revealed that Cas1 severely damaged plasma membranes in the chloroplast. Although the susceptibility of specific membrane lipids to Cas1 was not investigated sufficiently, these studies provided some evidence indicating that cytoplasmic membranes are highly susceptible to the pathogenicity of Cas1 [5,6]. The pathogenicity of Cas toxin to lipid membranes is probably similar to that of other mycotoxin classes infected in various hosts. For example, AK toxins from *Alternaria kikuchiana* were reported to severely damage cytoplasmic membranes in the leaves of Japanese pear. Simultaneously, fumonisins and AAL toxin from *Fusarium* species infecting crops and plants strongly disrupted sphingolipid metabolism in the plasma membrane of animal cells [16–19]. Objectively, no study has sufficiently clarified the susceptibility of phospholipids, glycerolipids, sterols, and betaine lipids available in plants [20–28] to the pathogenicity of Cas toxin.

Alternatively, plant resistance to infectious diseases is also known to be associated with several defense responses activated by host-pathogen interactions [29]. Recent transcriptomic analyses of the genetic responses of rubber clones susceptible and tolerant to *C. cassiicola* explored the diversity of genes encoding disease resistance proteins, leucine-rich repeat proteins, and genes involved in carbohydrate metabolic processes that were significantly upregulated in tolerant rubber clones upon infection. These genes, however, were either completely suppressed or downregulated in susceptible rubber clones [30]. Again, molecular phylogenetic studies failed to determine the key factor in the host selectivity of Cas toxin. The nature of the HST interaction of Cas toxin in CLF disease in different rubber clones remains elusive.

This study addressed several key questions to elucidate the HST interaction of Cas toxin and its cytotoxicity in CLF disease in rubber trees. Specifically, we examined the susceptibility of several important lipid components in plants to the pathogenicity of Cas1 and Cas2 isoforms

at the molecular and cellular levels by combining high-speed atomic force microscopy (HS-AFM), confocal microscopy, and cryo-scanning electron microscopy (Cryo-SEM), thereby clarifying the HST interaction of Cas1 and Cas2 isoforms to different plant lipids. At the cellular level, we examined the cytotoxicity of Cas1 and Cas2 on rubber leaves of RRIV 1, RRIV 4, and PB 255 clones to understand the HST interaction of Cas isoforms to specific hosts. Here, we report that the binding and disruption activities of Cas1 and Cas2 are more sensitive to negatively charged lipids (DPPA), glycerolipids (MGDG, DGDG), and phytosterol (stigmasterol) than to neutral (DPPC), sitosterol, and betaine lipids (DGTS-d9, DGTS). Cytotoxicity tests of Cas1 and Cas2 on rubber leaves of RRIV 1, RRIV 4, and PB 255 clones suggest that these clones are highly susceptible to the pathogenicity of Cas1 and Cas2 except for the strong resistance of PB 255 against Cas2. Finally, we also report that cytoplasmic membranes in susceptible rubber clones are highly vulnerable to the pathogenicity of Cas toxin.

Results and Discussion

Disruption activity of Cas1 and Cas2 to different lipid membranes imaged by HS-AFM

To examine the possible pathogenicity of Cas1 and Cas2, this study addressed the first question of whether Cas1 and Cas2 could bind to and disrupt various phospholipids (DPPC, DPPA), glycerolipids (MGDG, DGDG), sterols (stigmasterol, sitosterol), and betaine lipids (DGTS-d9, DGTS) available in plants. To answer this question, we used tapping-mode HS-AFM to image the dynamic interaction and disruption activities of Cas1 and Cas2 to different lipid membranes in real time. Unlike a conventional AFM, which has a slow scanning rate, HS-AFM can image in sub-second temporal resolution many biological molecules during functional activities [31–35]. The very soft and small cantilever used in HS-AFM was proven in numerous previous reports to non-invasively perturb the structures and functions of biological molecules [36–39]. This microscopy enables real-time, high-resolution imaging of individual biological nanomachines during their functional activities, as demonstrated by studies on walking myosin V [36], rotorless F1-ATPase [37], and actin filaments interacting with cofilin [38]. Most recently, this state-of-the-art technology has also been applied successfully to explore many undiscovered features of many other inspired biomolecules [39–45].

We produced Cas1 and Cas2 recombinant proteins in *E. coli*. The basic characteristics of these proteins are described in **Figures S1 – S2 and Table S1**. Our analysis predicted that a signal peptide (SP) domain in Cas1 and Cas2 containing several different hydrophobic amino acids (M, Y, L, I, A, F, V) may help to better insert these proteins into the hydrophobic region of a lipid bilayer. The numbers of negatively and positively charged residues in Cas1 and Cas2 are identical. However, the secondary structures (α-helix, β-sheet, and β-turn) in the mature domains of Cas1 and Cas2 are locally different (see red and yellow rectangles in **Figure S1**). To follow the binding and disruption activities of Cas1 and Cas2 on preformed lipid membranes in solution, Cas1 or Cas2 was added into the imaging chamber at a final concentration of 0.95

μM during HS-AFM imaging. Initially, we found that neutral phospholipid (DPPC) membranes were weakly sensitive to the binding and disruption activities of Cas1 and Cas2 (**Figures 1a1, a2**, **Table S2**, **Movies S1 – S2**). Thus, we made several composite lipid membranes by mixing with DPPC lipids to investigate their susceptibility to the pathogenicity of Cas1 and Cas2. As shown in **Figures 1b1, c1, d1, b2, c2, and d2, Table S2, and Movies S3 – S8**, the negatively charged phospholipid (DPPC/DPPA) and glycerolipid (DPPC/MGDG, DPPC/DGDG) mixtures were highly sensitive to the binding and disruption activities of Cas1 and Cas2. The DPPC/stigmasterol membranes were also strongly susceptible to the binding and disruption activities of both Cas1 and Cas2 (**Figures 1e1, e2, Table S2, and Movies S9 – S10**). Interestingly, other classes of phytosterol membrane mixtures (DPPC/sitosterol), however, showed different susceptibilities to Cas1 and Cas2. These membranes were highly vulnerable to Cas2 damage but weakly sensitive to Cas1 (**Figures 1f1, f2, Table S2, and Movies S11 – S12**). The lipid membrane mixtures of betaine lipids (DPPC/DGTS-d9, DPPC/DGTS) were weakly vulnerable to damage to Cas1 and Cas2 (**Figures 1g1, h1, g2, h2, Table S2, and Movies S13 – S16**).

In this study, our real-time HS-AFM imaging movies revealed that Cas1 and Cas2 were strongly bound to membranes containing negatively charged phospholipids (DPPA), glycerolipids (MGDG, DGDG), and sterol (stigmasterol) and penetrated deeply into the lipid membranes. Cas1 and Cas2 formed large clusters on these highly susceptible membrane lipids and expanded their clusters, similar to tsunamis, to devastate the membranes (**Figures 1b1, b2, c1, c2, d1, d2, e1, e2, and Movies S3 – S10**). By acting in these ways, they continuously damage lipid membranes. After disruption, many aggregates left on mica were observed. These aggregates were likely a mixture composed of lipids and Cas1 or Cas2. Our results also show that neutral DPPC lipids were weakly susceptible to the binding and disruption activity of both Cas1 and Cas2 (**Figures 1a1, a2, and Movies S1 – S2**). This statement is firmly supported in the observation of the disruption activity of Cas1 and Cas2 to DPPC domains and DGDG domains segregated in DPPC/DGDG membranes (**Figure 2B,2D, and Movies S7 – S8**). The DPPC and DGDG lipid domains formed on the mica surface were distinguished by a height difference of ~1.5 – 1.9 nm. Cas clusters were also distinguished by measuring the height differences with membranes and are representatively shown for Cas2 clusters (**Figure 2**). DGDG domains were strongly devastated by Cas1 and Cas2 clusters, while DPPC domains remained almost intact (kymographs in **Figures 2B and 2D**). Based on this observation, we further confirmed that glycerolipids (MGDG, DGDG) highly available in the cytoplasmic membrane of plant cells are strongly susceptible to the disruption activity of Cas1 and Cas2. Most likely, the negatively charged surface and high membrane fluidity of glycerolipids are two key factors for better binding, accessibility, and damage activity of Cas1 and Cas2 clusters in these membranes. We further tested membrane accessibility for the disruption activity of Cas1 and Cas2 by incorporating sterols (stigmasterol, sitosterol) into the membranes. The

presence of plant sterols in membranes was expected to increase the membrane accessibility for Cas1 and Cas2, although sterols are generally thought to decrease the membrane fluidity [25,26]. Indeed, these membranes were greatly devastated by Cas1 and Cas2 (**Figures 1e1,e2,f2, and Movies S9, S10, S12**), except for the weak disruption of DPPC/sitosterol caused by Cas1 (**Figure 1f1 and Movie S11**). Additionally, when neutral betaine lipids (DGTS-d9, DGTS) were mixed with DPPC lipids, these membranes were only weakly damaged by Cas1 and Cas2. The degrees of damage of Cas1 and Cas2 on these membranes were similar to those on pure DPPC membranes (**Figures 1a1,a2,g1,g2,h1,h2, and Movies S1 – S2, S13 – S16**). Overall, we suggest that negatively charged phospholipids and glycerolipids and specific sterols available in the cytoplasmic membranes of plant cells are strongly sensitive to the disruption activity of Cas1 and Cas2. Neutral phospholipids and betaine membrane lipids are weakly susceptible to the disruption activity of Cas1 and Cas2.

Binding of Cas1 and Cas2 to artificial cytoplasmic membranes imaged by confocal microscopy

We further examined the susceptibility of intact lipid membranes to the binding of Cas1 and Cas2 using confocal microscopy. Thus, we fabricated giant liposome vesicles (GVs) and used them as a model of artificial cytoplasmic membranes to assay the binding activities of GFP-Cas1 and GFP-Cas2. The composite GVs composed of similar lipid compositions used in HS-AFM observation were made by electroformation methods (**Table S3**). Confocal microscopy is a powerful imaging technique that has been successfully applied to study the binding of proteins to GVs [46,47]. Here, we mainly compared the binding of GFP-Cas1 and GFP-Cas2 to different GVs made of DPPC, DPPC/DPPA, DPPC/MGDG, DPPC/DGDG, DPPC/stigmasterol, DPPC/sitosterol, DPPC/DGTS-d9, and DPPC/DGTS lipid mixtures with the small addition of rhodamine-PE and biotinyl-PE lipids to absorb and image GVs.

Principally, we fabricated GVs containing both giant unilamellar and multilamellar vesicles and used them to assay the binding activity of GFP-Cas1 and GFP-Cas2 (**Figure 3, Table S4**). GVs gently maintained in the solution furnished perfectly suspended and intact lipid membrane-like artificial cytoplasmic membranes to assay the binding of GFP-Cas1 and GFP-Cas2. The binding of GFP-Cas1 and GFP-Cas2 to GVs made of only neutral phospholipids (DPPCs) was indeed weak (**Figures 3a1, a2, i1, i2**). Most DPPC GVs were not bound with GFP-Cas1 and GFP-Cas2. Thus, we used DPPC as the basal lipid membrane to compare the binding degrees of GFP-Cas1 and GFP-Cas2 to GVs composed of negatively charged phospholipids (DPPC/DPPA), glycerolipids (DPPC/MGDG, DPPC/DGDG), sterols (DPPC/stigmasterol, DPPC/sitosterol), and neutral betaine lipids (DPPC/DGTS-d9, DPPC/DGTS). GFP-Cas1 was bound more strongly to GVs composed of DPPC/DPPA, DPPC/MGDG, and DPPC/DGDG lipids than to GVs made of only DPPC (**Figures 3a1, b1, c1, d1, i1**). The susceptibility of GVs composed of DPPC/stigmasterol, DPPC/sitosterol,

DPPC/DGTS-d9, and DPPC/DGTS lipids to the binding of GFP-Cas1 was also recorded as strong (**Figures 3e1, f1, g1, h1**), although when compared to the binding of GFP-Cas1 to GVs made of only DPPC (**Figure a1**), the difference (p ≤ 0.05, *t-test*) was not significant (**Figure 3i1, Table S4**). Additionally, we found that GFP-Cas2 bound more strongly to all GVs composed of the negatively charged phospholipids, glycerolipids, sterols, and betaine lipids used in this study compared to GVs made of only the neutral DPPC phospholipids (**Figures 3a2, b2, c2, d2, e2, f2, g2, h2, i2**). These results strongly support that both GFP-Cas1 and GFP-Cas2 were bound to suspended lipid membranes, similar to artificial cytoplasmic membranes composed of different plant lipids. The susceptibility of the lipid membranes to the binding of GFP-Cas1 and GFP-Cas2 was varied and dependent on the types of lipids. Although we did not evaluate the disruption of these lipid membranes caused by GFP-Cas1 and GFP-Cas2 using confocal microscopy, we consistently captured the large clusters of GFP-Cas1 and GFP-Cas2 formed in the susceptible lipid membranes (see GFP fluorescence in **Figures 3b1, b2, c1, d1, e2, f2, g2, h2**). This observation also implies that the susceptible lipid components available in plants (PA, MGDG, DGDG, stigmasterol, and sitosterol) recruited the binding and formation of Cas1 and Cas2 clusters in the lipid membranes, as seen in our HS-AFM observation. Most likely, the formation and expansion of the large Cas1 and Cas2 clusters in susceptible lipid membranes play crucial roles in devastating lipid membranes.

Cytotoxicity of Cas1 and Cas2 on rubber leaves

To examine the cytotoxicity of Cas1 and Cas2 on rubber leaves at the cellular level, this study addressed the second question of whether Cas1 and Cas2 could directly damage and cause necrosis in rubber leaf tissues. Here, we tested the cytotoxicity of Cas1 and Cas2 on freshly detached young rubber leaves of highly susceptible clones (*H. brasiliensis* RRIV 1 and RRIV 4) and weakly susceptible clones (*H. brasiliensis* PB 255), as reported previously [11,13]. In these experiments, 6 – 10 small spots on a rubber leaf's lower lamina side were slightly scraped on the cuticle surface before applying 0.083 μg Cas1 or Cas2 to each spot. We evaluated the cytotoxicity of Cas1 and Cas2 on rubber leaves by observing the color change and the size change in the lesion spots. As seen in **Figure 4**, neither Cas1 nor Cas2 caused any noticeable damage or color change in the infected spots of all rubber leaves after incubation for 24 h. However, a green to brown color change was seen in some leaf lesion spots of susceptible RRIV 1 and RRIV 4 rubber clones infected with Cas1 and Cas2 after incubation for 72 h. The necrotic areas in the leaf lesion spots were largely expanded and seen after incubation for 120 h (**Figures 4a1, a2, b1, b2**). In the case of the PB 255 rubber clone, necrosis in the leaf lesion spots was developed and seen after treatment with Cas1 for 72 and 120 h (**Figure 4c1**). However, necrosis in the leaf lesion spots developed very slowly and was not clearly seen after treatment with Cas2 for 120 h (**Figure 4c2**). This observation suggests that the cytotoxicity of Cas1 and Cas2 on the rubber leaves of a PB 255 clone was different. Noticeably, some leaf

spots infected with Cas1 changed from green to brown and black colors (see black circles in **Figures 4a1, b1, c1**), while those infected with Cas2 only changed from green to brown color (**Figures 4a2, b2**). The blackened necrosis seen in lesion spots infected with Cas1 implies that Cas1 damaged leaf tissues more severely than Cas2. Once the damage of Cas1 and Cas2 on leaf tissues began, leaf tissue necrosis continuously developed and expanded in large areas. Overall, we demonstrated that both Cas1 and Cas2 could directly cause necrosis in the leaves of some rubber clones. Our report also supports the previous finding of the cytotoxicity of Cas1 produced in *C. cassiicola* resulting in necrosis in rubber leaves [1]. Indeed, the cytotoxicity of Cas2 on rubber leaves has never been reported before. Here, we additionally report that Cas2 directly damaged and caused necrosis in rubber leaves.

Dissecting cellular structures of rubber leaves using cryo-SEM
This study addressed the third question of how Cas toxin could damage cellular and tissue structures in rubber leaves. To answer this question, we used low voltage cryo-SEM to anatomize the cellular and tissue structures in the leaf lesion spots developed in rubber leaves of susceptible RRIV 4 clones after infection with Cas1 for ~120 h and compared them to the structures in healthy control leaves. Indeed, ultralow-temperature and low-voltage cryo-SEM has been proven to be a powerful technique for dissecting pristinely fractured biological cells without conductive metal coatings [48].

The lamina, cuticle, upper and lower epidermis, palisade, and spongy parenchyma in the healthy control leaves preserved their healthy cellular structures, which were identified easily (**Figures 5A, B, C, D, and S4A**). Additionally, intact cell walls and cytoplasmic membranes could be seen clearly in the fractured leaf tissues (**Figures 5C, D, and S4A**). In contrast, Cas1 strongly damaged the cellular and tissue structures in leaf lesion spots (**Figures 5E and S4B**). The upper and lower epidermis, spongy, and palisade parenchyma were devastated by Cas1. The cellular boundaries, such as cell walls and cytoplasmic membranes, in the fractured leaf tissues were hardly distinguished (**Figure S4B**). Strikingly, large areas of cytoplasmic membranes in palisade parenchyma were found to be severely devastated by Cas1 (**Figure 5E**). The binding of Cas1 clusters, pore formation, and expansion of Cas1 clusters at different degrees in the cytoplasmic membranes were clearly observed (see white rectangles in **Figure 5E**). Our results strongly suggest that cytoplasmic membranes were highly vulnerable to the pathogenicity of Cas1. This mechanism may also be similarly applied to understand the cytotoxicity of Cas2 on the leaves of susceptible rubber clones, although it needs to be verified.

Cytoplasmic membrane vulnerability to Cas toxin plays a crucial role in HST interactions
Cytoplasmic membranes are essential in all living cells. In plant cells, life strongly relies on the presence of a healthy functional cytoplasmic membrane enveloping the cytosol, thereby forming a boundary between the internal and external cytosolic environments. The cytoplasmic

membrane plays pivotal roles in protecting cytosolic contents, such as the chloroplast, Golgi apparatus, mitochondria, endoplasmic reticulum, and nucleus, and furnishing a sophisticated lipid environment for various vital activities across membranes, such as the transport activities of protein channels and transporters [49–51]. Rubber leaf tissue comprises the cuticle layers, lower and upper epidermis, palisade, and spongy parenchyma cells. Phospholipids (PC, PA), glycerolipids (MGDG, DGDG), sterols (stigmasterol, sitosterol), and betaine lipids (DGTS-d9, DGTS) are present in the cytoplasmic membranes of plant cells [20–28,53]. In the most relevant study on the vulnerability of cytoplasmic membranes to Cas1, the authors reported that purified Cas1 applied on rubber leaves could induce the same symptoms as the fungus did at the cellular level [5,6]. When observing the ultrastructures of the necrotic leaf tissues caused by Cas1, they found that Cas1 severely damaged the plasma membrane. Plasmolysis (e.g., membrane permeability) was modified. The authors also suggested that the neutral deuterated (^{2}H)DPC membrane was weakly susceptible to Cas1, although they could not rule out the interaction of Cas1 with other lipid classes [6].

In this study, we showed that both Cas1 and Cas2 could directly damage and cause necrosis in the leaves of some susceptible rubber clones. Our electron microscopic analyses strongly suggest that cytoplasmic membranes were highly vulnerable to the pathogenicity of Cas toxin (**Figures 5E and S4B**), supporting the previous finding that purified Cas1 could damage cytoplasmic membranes in chloroplasts [5,6]. The susceptibility of different lipids available in plants was systematically examined and clarified by combining HS-AFM and confocal microscopic observations. We explored here whether negatively charged phospholipids (DPPA), glycerolipids (MGDG, DGDG), and sterols (stigmasterol) available in cytoplasmic membranes play key roles in the binding and disruption activity of Cas1 and Cas2 to the cytoplasmic membrane. Neutral phospholipids (DPPC) and betaine lipids (DGTS-d9, DGTS) are indeed weakly sensitive to the disruption activities of Cas1 and Cas2. Our finding is crucial to understand the binding and disruption selectivity of Cas toxin to different lipid compositions in cytoplasmic membranes.

Studying the HST interaction of Cas isoforms with lipid membranes is crucial to understand the host-selective pathogen interactions in CLF diseases in different rubber clones. Currently, the exact mechanism remains unclear. In general, mycotoxins are categorized as host-specific or nonspecific toxins. Some plant pathogenic fungi can synthesize mycotoxins as secondary metabolites that act as virulence factors to develop severe fungal infections [18,53,54]. Several important organelles inside plant cells, such as the cytoplasmic membrane, chloroplasts, mitochondria, and endoplasmic reticulum, have previously been suggested as target sites of selective AK toxins (reviewed in Tsuge et al., [19]). In particular, selective AK and fumonisin toxins were reported to damage or modify cytoplasmic membranes in various ways [16,17]. In this study, we demonstrated that Cas1 and Cas2 were directly damaged and caused necrosis in the leaves of susceptible rubber clones (RRIV 1, RRIV 4, and PB 255). RRIV 1 and RRIV 4 clones

were sensitive to both Cas1 and Cas2 (**Figures 4a1, a2, b1, b2**). Strikingly, a PB 255 clone was strongly resistant to Cas2 but susceptible to Cas1 (**Figures 4c1, c2**). These results may suggest that the HST interaction of the Cas1 and Cas2 isoforms varied in different rubber clones, depending on the susceptibility of cytoplasmic membranes to the binding and disruption of Cas toxin. We suggest here that the cytotoxicity mechanism of Cas1 and Cas2 is universally applied to understand the host-selective toxic interaction of other selective Cas isoforms (Cas3 to Cas6) and mycotoxins with specific lipid membranes.

Conclusions

In this study, we combined HS-AFM, confocal microscopy, cryo-SEM, and cytotoxicity assays to analyze the HST interaction of Cas1 and Cas2 isoforms with different lipid membranes and the cytotoxicity of these toxins on cytoplasmic membranes at the molecular and cellular levels. Our HS-AFM analyses unveil the selective binding and disruption activities of Cas1 and Cas2 to lipid membranes that are strongly dependent on the types of lipids available in the cytoplasmic membranes of plant cells. Negative lipids (DPPA), glycerolipids (MGDG and DGDG), and sterols (stigmasterol) were strongly susceptible to the binding and disruption activity of Cas1 and Cas2. Neutral lipids (DPPC), sitosterol, and betaine lipids (DGTS-d9 and DGTS) were weakly sensitive to the disruption of Cas1 and Cas2. Using a model of artificial cytoplasmic membranes (i.e., GVs) composed of similar plant lipids used in HS-AFM observation, our confocal microscopic analyses consistently reveal the strong susceptibility of negative lipids, glycerolipids, and sterols to the binding and cluster formation of Cas1 and Cas2. We consistently confirmed that neutral phospholipids were indeed weakly susceptible to the binding of both Cas1 and Cas2. The susceptibility of sitosterol and neutral betaine lipids to the binding of Cas1 and Cas2 somehow differs between our HS-AFM and confocal microscopic analyses (**Table S2**). Regardless of the weak disruption activities of Cas1 and Cas2 on these lipid membranes seen by HS-AFM observation, Cas2 showed stronger binding to these lipid membranes than Cas1 did when the binding assays were examined using a model of artificial cytoplasmic membranes (GVs). Furthermore, the cytotoxicity of Cas2 on rubber leaves has not been reported before. Here, our cytotoxicity tests of Cas1 and Cas2 on rubber leaves of RRIV 1, RRIV 4, and PB 255 clones suggest that Cas1 and Cas2 directly damaged and caused necrosis in the leaves of these rubber clones except for the strong resistance of a PB 255 clone against Cas2. Finally, our electron microscopic analyses also reveal that cytoplasmic membranes in rubber leaves are highly susceptible to the pathogenicity of Cas toxin. Cytoplasmic membrane vulnerability to Cas toxin is the most remarkable feature of Cas toxin cytotoxicity against plant cells. These findings may strongly relate to the HST interaction of Cas toxin with specific lipid membrane compositions in plant cells.

Methods

Materials

DNA oligonucleotides encoding cassiicolin (Cas) genes (Cas1 and Cas2) of *Corynespora cassiicola* causing CLF disease in rubber trees [7,9,15] were purchased from IDT (Tokyo Japan). The PcoldGFP plasmid was a generous gift from Prof. Taro Q.P. Uyeda (Waseda University, Japan). All necessary primers used for PCR and cloning Cas1, Cas2, GFP-Cas1, and GFP-Cas2 were purchased from Macrogen Japan (Tokyo, Japan). The oligonucleotides and amino acid sequences of Cas1 and Cas2 used in this study are summarized in **Table S5**. All synthetic lipids available in plants were purchased from Avanti Polar Lipids (Alabama, USA). The structures and physical properties of these lipids are clarified and summarized in **Figure S3**.

Protein preparation

The genes encoding Cas1 and Cas2 proteins were similarly inserted into the pColdI vector at the *KpnI* and *XbaI* sites [38]. Similarly, the PcoldGFP vector (generated two cloning sites by *BamHI* and *HindIII*) was employed to construct GFP-Cas1 and GFP-Cas2 proteins. The successfully constructed plasmids for the expression of Cas1, Cas2, GFP-Cas1, and GFP-Cas2 genes were confirmed by DNA oligonucleotide sequences. All recombinant proteins containing a 6xHis-tag on the N-terminus (**Table S5**) were designed for purification using a Ni-NTA resin column. For simplicity, we consistently designated these recombinant proteins as Cas1, Cas2, GFP-Cas1, and GFP-Cas2.

Cas1, Cas2, GFP-Cas1, and GFP-Cas2 were expressed in BL21 (DE3) *E. coli* according to the manufacturer's instructions for PcoldI (Takara). Briefly, the transfected *E. coli* cells were grown in LB broth containing 100 µg/ml ampicillin and 10 µg/ml methyl 3-O(alpha-D-mannopyranosyl)-alpha-D-mannopyranoside (MDMDM) to an OD600 of ~ 0.6. Then, the cell suspension was cooled to 15°C on ice. Protein expression was induced by adding 1 mM IPTG. The cell suspension was continuously fermented in a shaking incubator at 140 rpm and 15°C for 24 h. Then, the cells were harvested by low centrifugation (4000 rpm, 10 min, 4°C). The cell pellet was gently washed twice with cold 10 mM Tris-HCl buffer (pH 7.4). Next, the cell pellet was resuspended in lysis buffer containing 50 mM Tris-HCl buffer (pH 8.0), 300 mM KCl, 5 mM EGTA, 20 mM imidazole (pH 7.4), 1% (w/v) lauryl maltose neopentyl glycol (LMNG) (Anatrace), 10 mM β-mercaptoethanol, proteinase inhibitor cocktail (Sigma), and 1 mM PMSF. Cell lysis was carried out overnight in a rotary incubator at 4°C. Next, the cells were finally disrupted using a French press (repeated twice, ~140 MPa). After low centrifugation (15,000 rpm, 15 min, 4°C), the crude protein solution was finally collected by ultracentrifugation (40,000 rpm, 30 min, 4°C) and subsequently incubated with Ni-NTA (GE healthcare) resin for 2 h at 4°C. The resin was recovered and transferred into a clean plastic column for washing. The resin was washed carefully in cold wash buffer containing 10 mM Tris-HCl (pH 7.4), 20 mM imidazole (pH 7.4), 1 M NaCl and 10 mM β-mercaptoethanol until

proteins in the washout solution were undetectable. Elution of proteins was carried out with elution buffer containing 10 mM Tris-HCl (pH 7.4), 800 mM imidazole (pH 7.4) and 10 mM β-mercaptoethanol. The eluate was dialyzed against dialysis buffer containing 10 mM Tris-HCl (pH 7.4), 50 mM KCl, 50% glycerol, and 10 mM β-mercaptoethanol using a dialysis membrane (MWCO 3300 Da) overnight at 4°C. The dialysate was recovered and concentrated and finally subjected to low centrifugation (15,000 rpm, 10 min, 4°C) to remove any protein aggregates. Protein concentration was measured by the Bradford method or UV absorption (Cas1: ε_{280} = 8855 $M^{-1} \cdot cm^{-1}$ or A_{280} = 0.984 (1 mg/ml), 9003.27 Da; Cas2: ε_{280} = 8855 $M^{-1} \cdot cm^{-1}$ or A_{280} = 0.981 (1 mg/ml), 9025.28 Da; GFP-Cas1: ε_{280} = 29380 $M^{-1} \cdot cm^{-1}$ or A_{280} = 0.830 (1 mg/ml), 35400.95 KDa; GFP-Cas2: ε_{280} = 29380 $M^{-1} \cdot cm^{-1}$ or A_{280} = 0.815 (1 mg/ml), 35422.07 KDa). Small aliquots of proteins were snap-frozen in liquid nitrogen and stored at -80°C. The activities of target proteins were characterized by common biochemical assays, mass spectrometry, HS-AFM, confocal microscopy, cryo-SEM, and cytotoxicity assays on rubber leaves.

Giant liposome vesicles

We made giant liposome vesicles (GVs) from different lipids available in plants for imaging the binding of GFP-Cas1 and GFP-Cas2 to different lipid membranes using confocal microscopy. The electroformation methods for making GVs have been well established in several previous studies [55–57]. The lipid compositions are described in **Table S3** and clarified in **Figure S3**. Briefly, the lipid mixtures dissolved in chloroform were stored at -20°C. The mixtures were warmed at room temperature for 10 min. A 20 µl lipid mixture was thoroughly spread on indium tin oxide (ITO)-coated glass slides (Nanion, Germany). The dried thin film was formed by the complete evaporation of chloroform at room temperature for approximately 10 min. To make GVs on the ITO-coated glass slide, we used a Vesicle Prep Pro (Nanion, Germany). An O-ring with a diameter of 16 mm was used to make a chamber furnishing the dried thin film inside. A 250 µl filter sterile electroformation buffer containing 1 M D-sorbitol, 1 mM EGTA, and 2 mM HEPES-NaOH (pH 7.4) was applied into a chamber sandwiched between two conductive sides of the ITO-coated glass slides. The protocol for making GVs was set up as follows: Initial (0 V, 5 Hz, 50°C, 5 min); Start (3 V, 10 Hz, 50°C, 10 min); Main (3 V, 10 Hz, 50°C, 60 min); Fall (0 V, 10 Hz, 50°C, 5 min); End (0 V, 10 Hz, 20°C). The formed GVs were gently collected and stably stored at 4°C for approximately 1 – 2 weeks.

Confocal microscopy

The FluoroDish cell culture dishes (FD35-100, WPI) were cleaned by dipping in 3 M KOH solution for 1 h, subsequently washed in Milli-Q water approximately 10 times, dried at 60°C for 1 h or more, and stored at room temperature before use. GV solution (~0.8 mM lipid) was diluted in imaging buffer containing 5 mM HEPES-NaOH (pH 7.4), 5 mM NaCl, 0.05 mM

EDTA, and 1 M D-sorbitol to a final lipid concentration of ~0.2 mM. To assay the binding of Cas1 or Cas2 to different lipid membranes, we gently mixed 9.5 µM GFP-Cas1 or GFP-Cas2 with 100 µl of diluted GV solution, incubated the mixture at room temperature for 5 min, and subsequently introduced the mixture into a cleaned FluoroDish. In most cases, we could image the GVs weakly absorbing onto the glass surface by gravity force. Only in the case of negatively charged DPPC/DPPA GVs did we further added 300 mM NaCl and 10 mM $MgCl_2$ into the imaging buffer for better absorption of these GVs onto the glass surface.

Confocal imaging experiments were performed in a STED confocal microscopy (Abberior Instruments, Germany). We used a 100x oil-immersed objective lens (NA=1.46). Images were taken using Imspector software. Two channel images were acquired one by one for each pixel at 50 x 50 x50 nm resolution per xyz pixel. The confocal imaging conditions were set up as follows: SiR channel (Ex: 652 nm) for rhodamine, EGFP channel (Ex: 489 nm) for GFP, 15% laser power source used for both channels. The images were analyzed using Fiji-ImageJ (NIH, USA). Initially, we corrected the background for both channels. After a Gaussian-blur filter (sigma radius = 2.0) was applied, the images were converted to binary images with a minimum threshold set value of 12 for measuring the pixel areas in each channel. The rhodamine area where Cas is not bound was calculated by subtracting the GFP channel from the rhodamine channel. Then, the relative fluorescence area was calculated for a quantitative comparison of the binding area of GFP-Cas1 and GFP-Cas2 to different GVs.

Mass spectrometry

The target Cas1 protein band was excised from the electrophoresis gel and subjected to in-gel digestion [58]. The peptide fractions were analyzed by a solariX (Bruker Daltonics, Billerica, USA), as previously described [59].

High-speed atomic force microscopy

We used a laboratory-built high-speed atomic force microscope (HS-AFM) as described previously [31,33,38]. HS-AFM imaging was carried out in solution using tapping mode with small cantilevers (BL-AC10DS-A2, Olympus, Tokyo, Japan) whose spring constant, resonant frequency in water, and quality factor in water were ~0.1 N/m, ~500 kHz, and ~1.5, respectively. Our lab-made ferrocene tip on an original tip-less cantilever was grown through electron beam deposition (EBD) using scanning electron microscopy (ZEISS Supra 40 VP/Gemini column, Zeiss, Germany). Typically, the EBD tip was grown under vacuum (1 – 5 x 10^{-6} Torr), aperture size (10 µm), and EHT voltage (20 kV) for 30 s. The EBD ferrocene tip was further sharpened using a radio frequency plasma etcher (Tergeo Plasma Cleaner, Pie Scientific, CA, USA) under an argon gas atmosphere (typically at 180 mTorr and 20 W for 30 s). During HS-AFM imaging, the free-oscillation peak-to-peak amplitude of the cantilever (A_0) was set to ~1.6 – 1.8 nm, and the feedback amplitude set-point was set at ~$0.9A_0$.

Real-time imaging of disruption of lipid membranes caused by Cas1 and Cas2

We prepared small unilamellar vesicles (SUVs) or liposomes by the thin-film hydration method and mica-supported lipid bilayer as described previously [38]. In this study, DPPC, DPPC/DPPA (80/20 wt%), DPPC/MGDG (80/20 wt%), DPPC/DGDG (60/40 wt%), DPPC/stigmasterol (80/20 wt%), DPPC/sitosterol (80/20 wt%), DPPC/DGTS-d9 (80/20 wt%), and DPPC/DGTS (80/20 wt%) liposomes were made. Typically, liposomes were made in Milli-Q water at 1 mg/ml and stored at $-20°C$. To form a lipid bilayer on mica, liposomes were diluted in 10 mM $MgCl_2$ to 0.1 mg/ml and sonicated with a bath sonicator at room temperature (AUC-06 L, AS ONE, Osaka, Japan) for 1 min. Then, 2 µl of the sonicated liposomes was deposited on the surface of freshly cleaved mica (2 mm in diameter), which had been glued onto a glass stage beforehand, and incubated for approximately 2 h at room temperature ($24 - 26°C$) in a humid sealed container to avoid surface drying.

Real-time imaging of the binding and disruption activities of Cas1 and Cas2 to lipid membranes formed on mica was carried out in C-buffer containing 10 mM HEPES-NaOH (pH 7.4), 0.1 mM EDTA, and 100 mM NaCl at room temperature by using HS-AFM. In all HS-AFM experiments, we consistently used 0.95 µM Cas1 or Cas2 as a final concentration to examine the susceptibility of different lipid membrane compositions to Cas1 and Cas2. The sample volume in the HS-AFM imaging experiment was ~70 µl.

Cytotoxicity on rubber leaves caused by Cas1 and Cas2

Young and healthy leaves of rubber trees (*H. brasiliensis* RRIV 4, RRIV 1, and PB 255 clones) grown in southern Vietnam were freshly collected in the early morning. It usually took $4 - 5$ h before a cytotoxicity test. The leaves were carefully disinfected with 60% ethanol and sterilized Milli-Q water. Three rubber leaves were placed on a plastic net under one experimental condition and separately incubated inside a plastic box (40 cm x 40 cm x 5 cm). The moisture was maintained by laying down wet Whatman filter paper under a plastic net, avoiding direct contact with leaves. To test the cytotoxicity of Cas1 and Cas2 on rubber leaves, 6 to 10 small spots on the lower lamina sides of leaves were chosen and slightly scraped on the cuticle wax layer with a small pipette tip. Next, 10 µl of 0.0083 µg/µl (~ 0.083 µg) Cas1 or Cas2 was applied to each spot. The molar concentration of Cas1 and Cas2 infected in each spot was kept almost the same as that used for HS-AFM observation, although the final sample volume used in HS-AFM observation was ~ 7 times higher. The control experiments were performed similarly by applying 10 µl of sterilized Milli-Q water to each spot. The control and infected leaf samples were separately incubated and maintained under the same humidity (~80 – 90%) and temperature (~26 – 28°C) in the dark. For sample analyses, leaves in each moist plastic box were carefully photographed after 24, 72, and 120 h of infection by using a conventional digital camera. Each experimental condition was repeated 2 – 3 times. The leaf lesion spots

caused by Cas1 and Cas2 on different rubber clones were compared by observing color changes and lesion size and dissecting the cellular structures by cryo-SEM.

Cryo-SEM imaging

We selected the healthy (control, + water, 120 h) and infected (+ Cas1, 120 h) leaves of one rubber clone (RRIV 4) to anatomize the leaf tissues and cellular structures. To make the Cryo-SEM samples, healthy and lesion-containing areas surrounding the initially scraped spots were chosen. The ultrastructures of leaf tissues were analyzed by low voltage cryo-scanning electron microscopy (Cryo-SEM), a powerful technique for imaging pristinely fractured biological cells without conductive metal coating [48]. Leaf samples were punched out with a 3 mm diameter circular blade and plunged into liquid ethane at 90 K. Cryo-SEM images were obtained from a Helios G4 CX (Thermo Fisher Scientific, USA) with a PP3010 Cryo-SEM transfer system (Quorum Technologies, UK). Frozen leaf samples were clamped perpendicular at the top and the center of a metal cylinder on the transfer shuttle and fractured inside the vacuum chamber to face the freshly fractured depth profile just on the top of the cylinder without conductive metal coating. No ice contamination growth was visible during the fracture of samples under high vacuum conditions below a pressure of 5.0×10^{-5} Pa. The sample stage temperature was kept at 93 K. A 1 kV electron beam of the landing energy with a stage bias voltage of 2 kV was used substantially in low voltage cryo-SEM imaging of the fractured sample surfaces embedded in a cylindrical shape holder. Notably, only when the lower lamina side of rubber leaves was imaged we coated the leaf surface with platinum in the vacuum chamber before imaging.

Analyses of HS-AFM images

HS-AFM images were viewed, analyzed, and exported by using the laboratory built software Kodec4.4.7.39. Kodec4.4.7.39 software was coded in Visual C# (Visual Studio 2010, Microsoft, USA), and source code 1 is openly available [38]. All filters and subroutines for image analyses used in the present study were included in the software. We confirmed the compatibility between the software and computers operated with Windows 8 or 10. This software should be cited as Sakashita M, M Imai, N Kodera, D Maruyama, H Watanabe, Y Moriguchi, and T Ando. 2013. Kodec4.4.7.39. Briefly, AFM images were flattened and filtered (Gaussian blur, Sigma radius: 1 nm) to increase the S/N ratio. AFM images were converted and extracted to BMP format images. The image sequences were converted to a movie format (AVI) using Fiji-ImageJ software (NIH, USA).

Statistics

All data (mean ± SD) were statistically processed using an Origin Pro 2016 graphic software (OriginLab, USA). The differences were statistically tested using two-independent populations

t-test.

Author contributions

KXN and NBQ designed concepts. KXN designed and constructed plasmids, and KXN, NDNP, TOM expressed, purified, and analyzed proteins. NBQ, NDNP, NNBC, NPV, and NAN performed the cytotoxicity test. KXN and NDNP performed HS-AFM imaging. HF, KXN, and NBQ performed cryo-SEM observation and analyzed data. TS, MM, and KXN performed mass spectrometry and analyzed data. KXN, TI, and TF performed confocal microscopy. KXN, NDNP, NK, TA, HK, and NBQ analyzed HS-AFM data. KXN, NBQ, and TA wrote the manuscript.

Competing interest statement

The authors declare no competing interests.

Nomenclature

DPPC: 1,2-dipalmitoyl-sn-glycero-3-phosphocholine

DPPA: 1,2-dipalmitoyl-sn-glycero-3-phosphate

MGDG: Monogalactosyldiacylglycerol

DGDG: Digalactosyldiacylglycerol

DGTS-d9: 1,2-dipalmitoyl-sn-glycero-3-O-4'-[N,N,N-trimethyl(d9)]-betaine

DGTS: 1,2-dipalmitoyl-sn-glycero-3-O-4'-(N,N,N-trimethyl)-betaine

GVs: giant liposome vesicles

Cas: cassiicolin

CLF: corynespora leaf fall

CCP: pathogenic *C. cassiicola* isolates in rubber trees originally from the Philippines

HS-AFM: High-speed atomic force microscopy

Cryo-SEM: cryo-scanning electron microscopy

MALDI FT-ICR: matrix-assisted laser desorption/ionization Fourier-transform ion cyclotron

resonance

IPTG: Isopropyl β-D-1-thiogalactopyranoside

PMSF: Phenylmethylsulfonyl fluoride

MWCO: Molecular weight cutoff

RRIV: Rubber research institute of Vietnam

PB: Prang Besar (a name of a rubber research center in Malaysia)
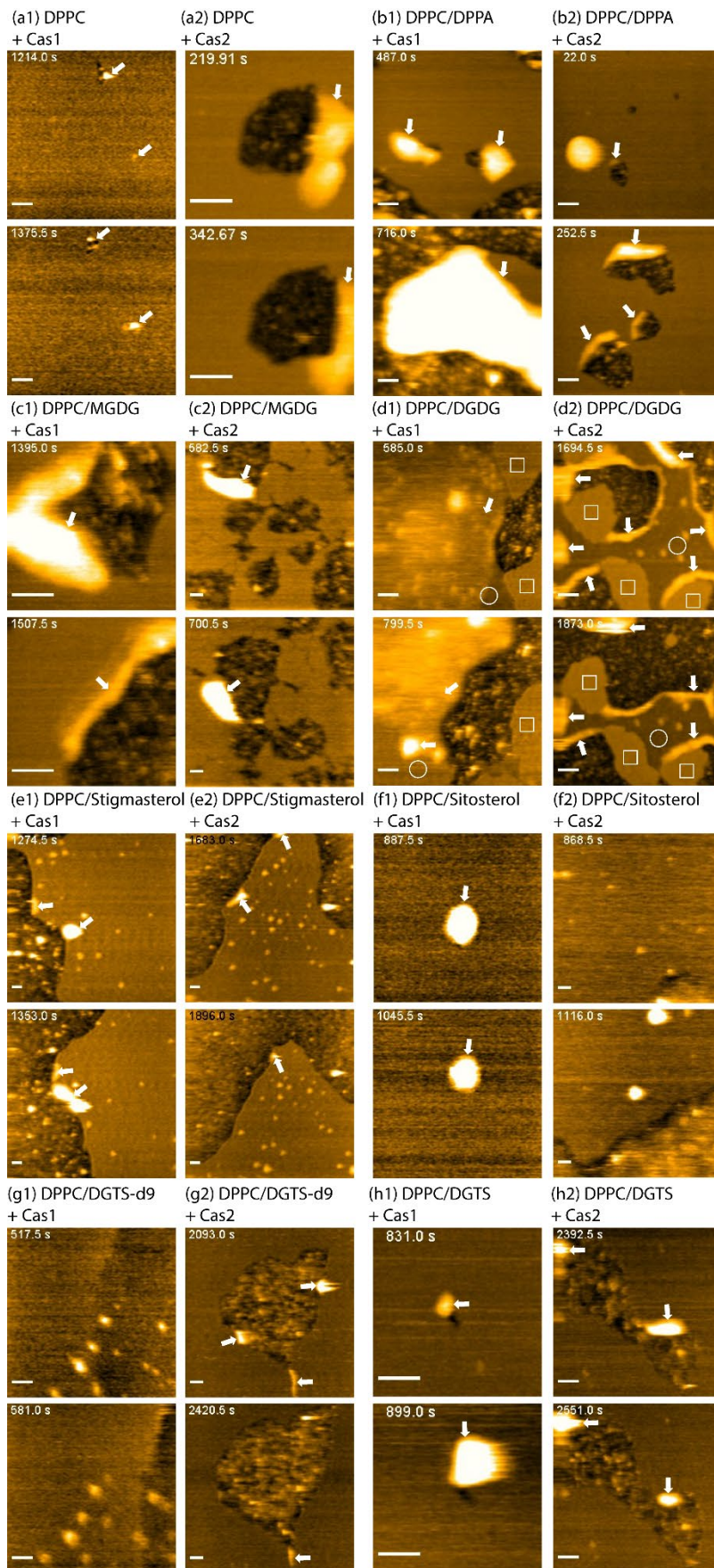
Figure 1. HS-AFM imaging of disruption processes of different membrane lipids available in

plants induced by Cas1 and Cas2. Briefly, lipid bilayers consisting of different lipid compositions were formed on mica by rupturing liposomes. Then, 0.95 µM Cas1 or Cas2 was added, and HS-AFM imaging was carried out in C-buffer using a BL-AC10DS-A2 cantilever deposited with a small lab-made tip. White arrows: Cas1 and Cas2 clusters directly incorporated into the lipid bilayer. Rectangles and circles in d1 and d2 denote DPPC and DGDG domains, respectively. Imaging rate: 2 fps. The time label in still images denotes a time point after the addition of Cas1 or Cas2. Bars: 50 nm. **Related to Movies S1 – S16, and Table S2**.
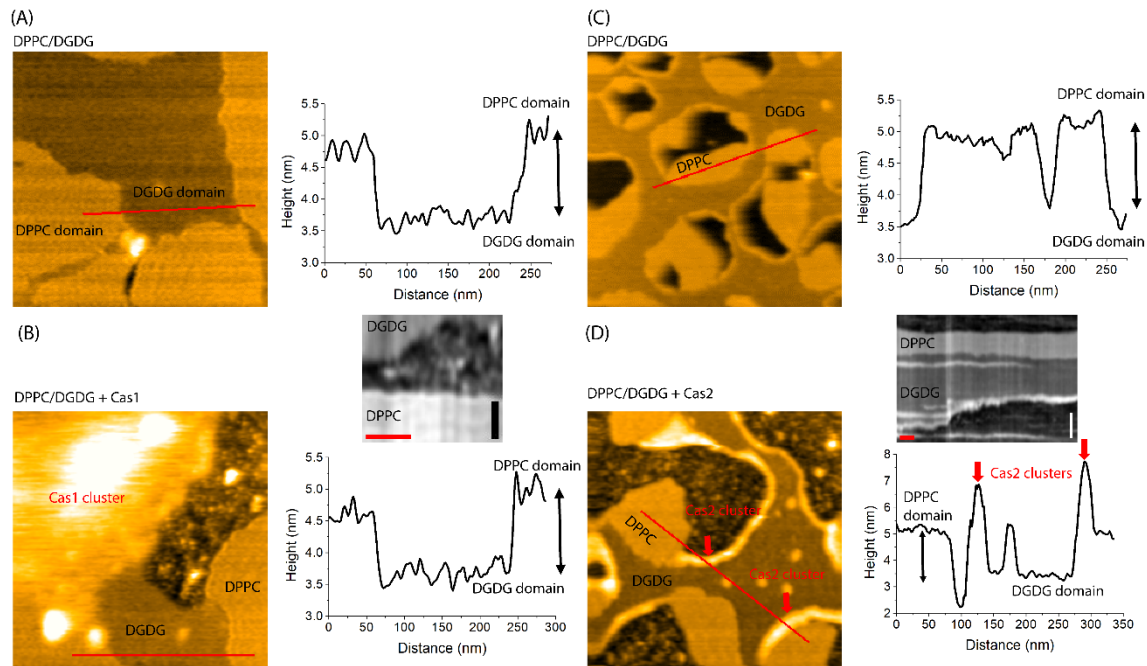
Figure 2. HS-AFM topographic image analyses. (A, B) HS-AFM images of the DPPC/DGDG lipid bilayer formed on mica in the absence and presence of Cas1 (left) and cross-sectional profiles and typical kymographs (right). (C, D) HS-AFM images of the DPPC/DGDG lipid bilayer formed on mica in the absence and presence of Cas2 (left) and cross-sectional profiles and typical kymographs (right). DPPC, DGDG, and Cas clusters were distinguished by height differences. Red bars: 20 s, black and white bars: 50 nm. **Related to Figures 1d1 – d2 and Movies S7 – S8.**
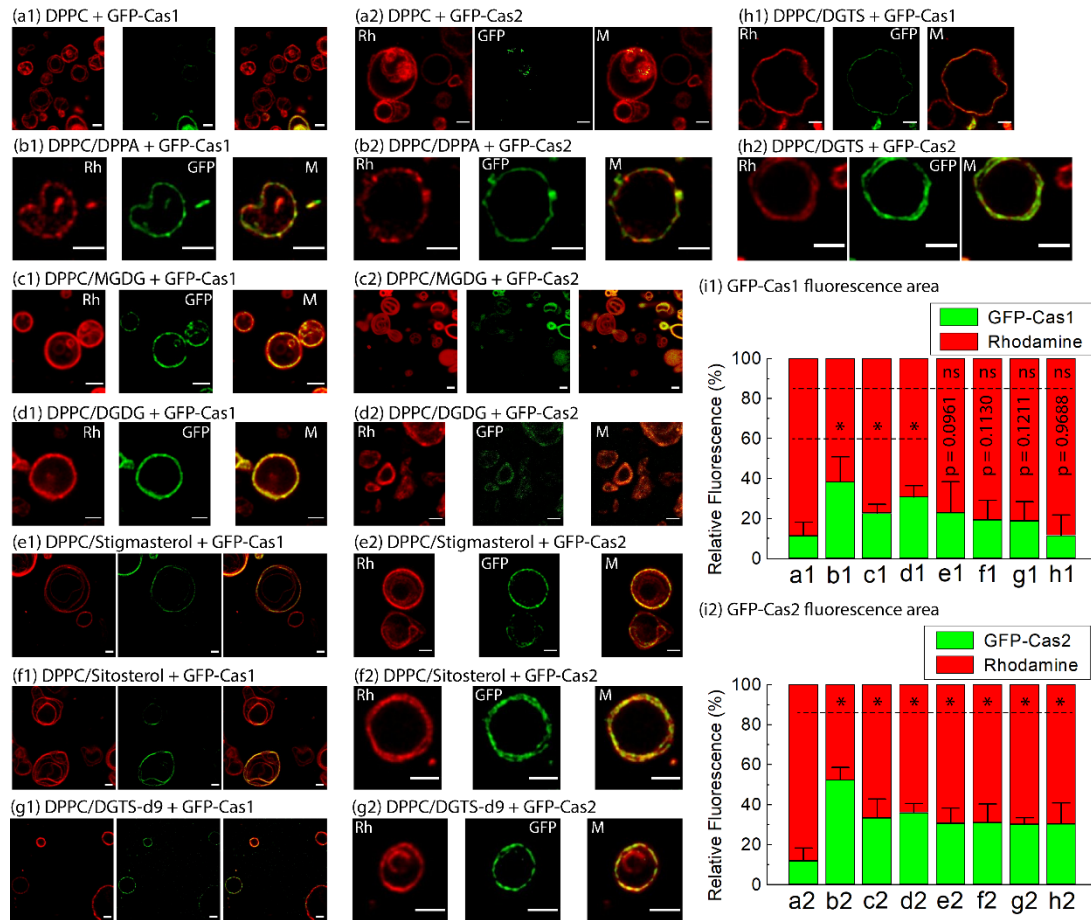
Figure 3. Confocal microscopic imaging to quantify the binding of GFP-Cas1 and GFP-Cas2 to GVs made of different lipids available in plants. The final concentration of GFP-Cas1 and GFP-Cas2 was 9.5 µM. From left to right (a1 – h1, a2 – h2), Rh: rhodamine-PE, GFP: GFP-Cas1 or GFP-Cas2, M: merged. Bars: 5 µm. (i1 and i2) Quantification of relative fluorescence areas of GFP-Cas1 and GFP-Cas2 on various GVs described from a-h. The values are mean ± SD. GFP fluorescence areas on DPPC GVs were used as the controls for comparison with those on other GVs. Asterisks (*) show a significant difference (p ≤ 0.05, two-independent populations *t-test*). *p*-values are shown when the difference is not significant (ns) at the indicated level (p ≤ 0.05). Number of values in each population: 6 – 11. **Related to Tables S2 and S4**.
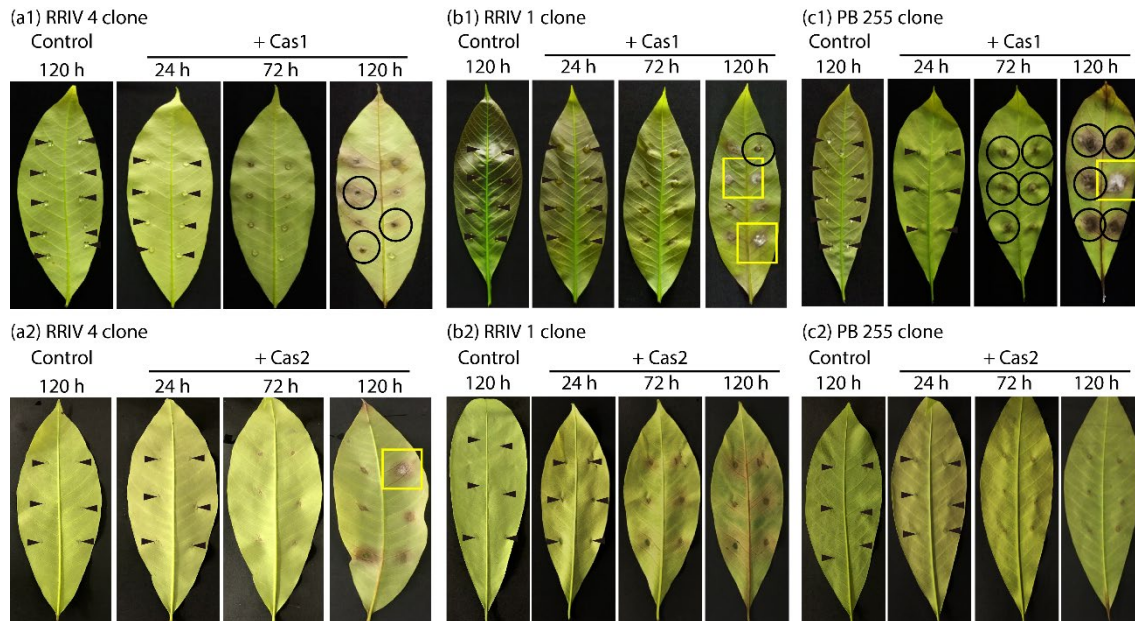
Figure 4. Cytotoxicity of rubber leaves of RRIV 4, RRIV 1, and PB 255 clones caused by Cas1 and Cas2. Six to ten small spots on the lower lamina sides of the healthy rubber leaves were slightly scraped before cytotoxicity tests. Control: Ten microliters of sterilized water was applied to each spot. Infected leaves: Ten microliters of 0.0083 µg/µl (~0.083 µg) Cas1 or Cas2 was applied to each spot. Control and infected leaves were separately incubated under the same humidity (~80 – 90%) and temperature (26 – 28°C) and photographed after incubation at 24, 72, and 120 h by a conventional digital camera. Arrowheads: Initial positions of the infected spots. Black circles: blackened lesion spots: Rectangles: possible contamination of fungi. **Related to Figure 5 and Figure S4**.
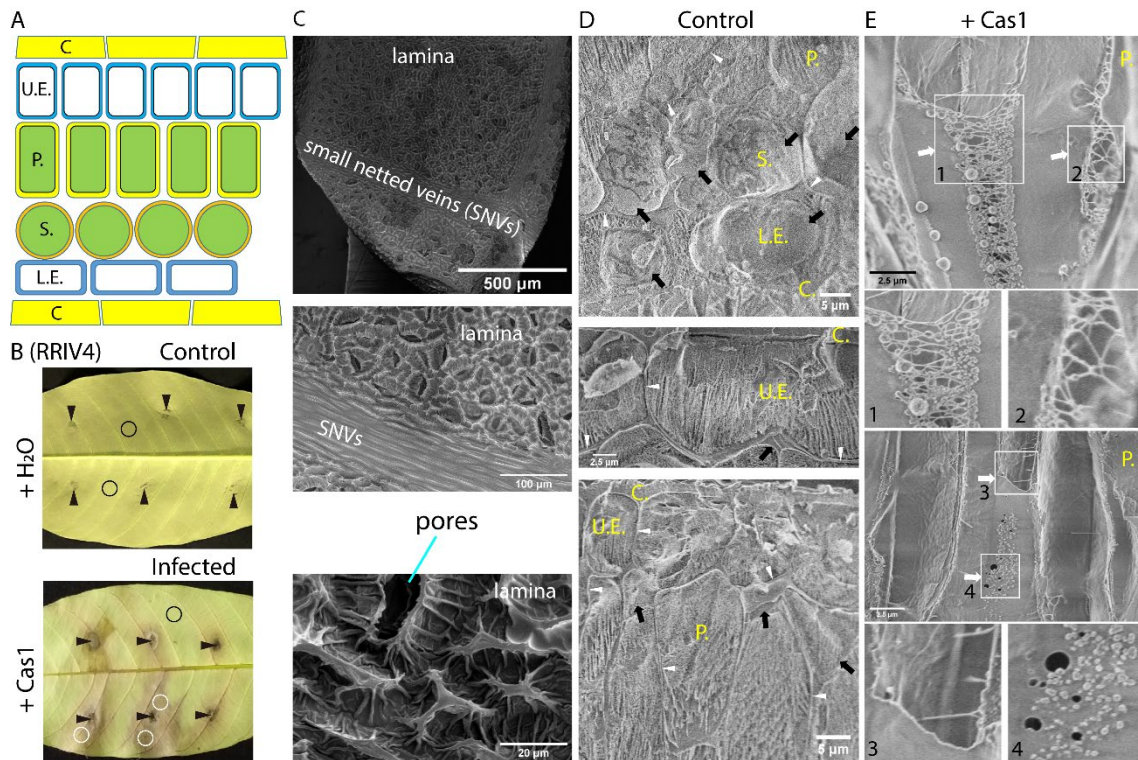
Figure 5. Cryo-SEM images of cellular and tissue structures of healthy controls and lesion spots in rubber leaves (RRIV 4 clone) caused by Cas1. (**A**) An illustration of leaf tissue anatomy; (**B**) Lower lamina side of the healthy control and infected rubber leaves (+ 0.083 µg Cas1) after incubation for ~ 120 h. The small areas of the healthy control (black circles) and lesion spots (white circles) in rubber leaves shown in B were punched out and plunged into liquid ethane, and cellular and tissue structures were dissected. Black arrowheads: initially infected spots. (**C**) Lower lamina side of rubber leaves. (**D, E**) Cellular and tissue structures of the healthy control and lesion spots. Black and white arrows denote the healthy and damaged cytoplasmic membranes, respectively. White arrowheads: the cell wall. C: cuticle, U.E.: upper epidermis, L.E.: lower epidermis, P.: palisade, S.: spongy. **Related to Figure 4 and Figure S4**.
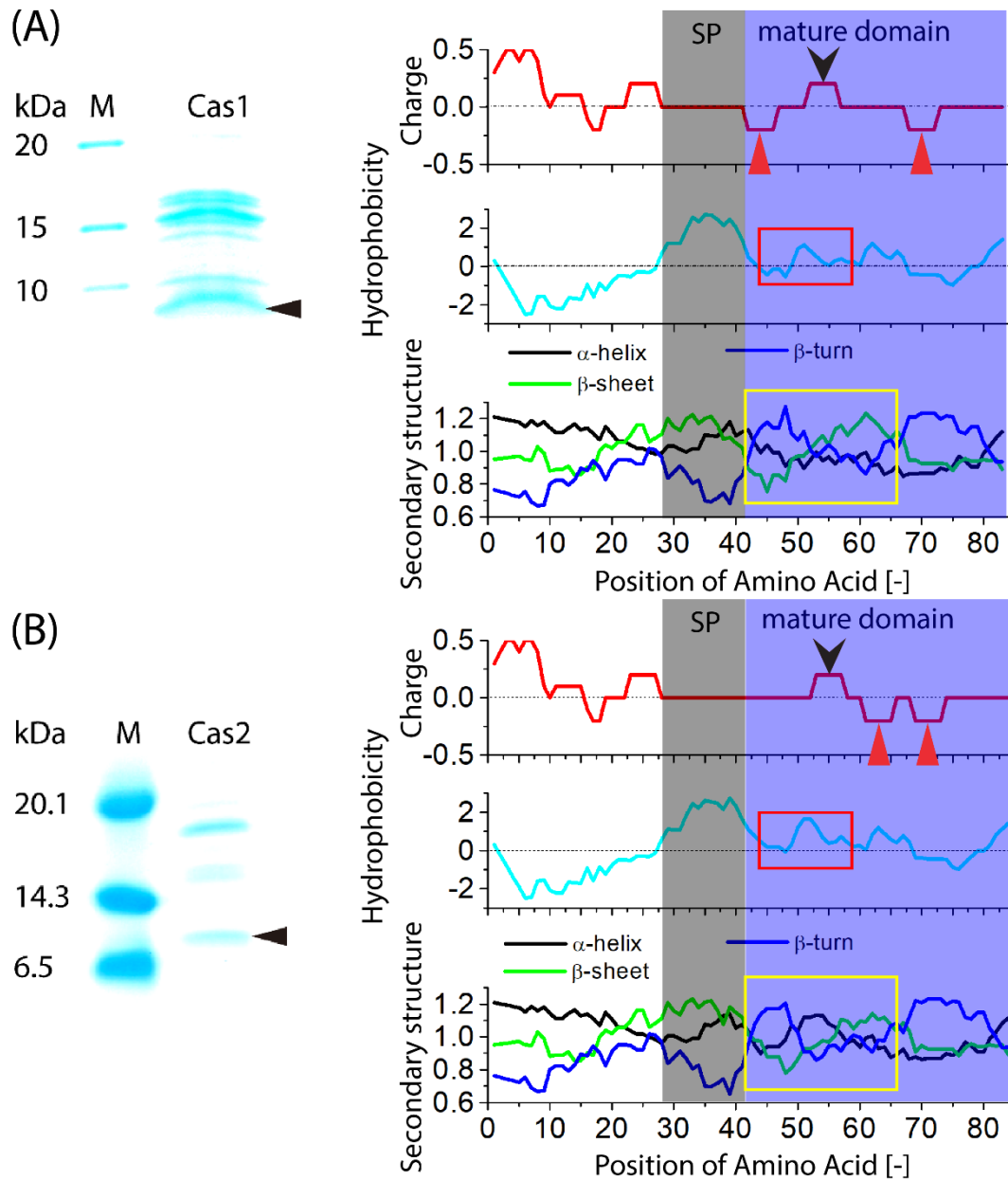
Figure S1. Purification of Cas1 and Cas2 from *E. coli*. (**A**) SDS-PAGE gel images of Cas1 and Cas2 stained with Coomassie Brilliant Blue R-250 (CBB) (**B**) Computing charge (http://www.bioinformatics.nl/cgi-bin/emboss/charge), hydrophobicity, and secondary structure (alpha-helix, beta-sheet, and beta-turn) scales based on the profiles produced by amino acid sequences of Cas1 and Cas2 (https://web.expasy.org/protscale/). SP: signal peptide; red and black arrowheads show the positions of the negatively and positively charged amino acids, respectively, in mature domains; red and yellow rectangles show the regions in which the hydrophobicity and secondary structure of Cas1 and Cas2 may differ. **Related to Figure S2 and Table S1**.
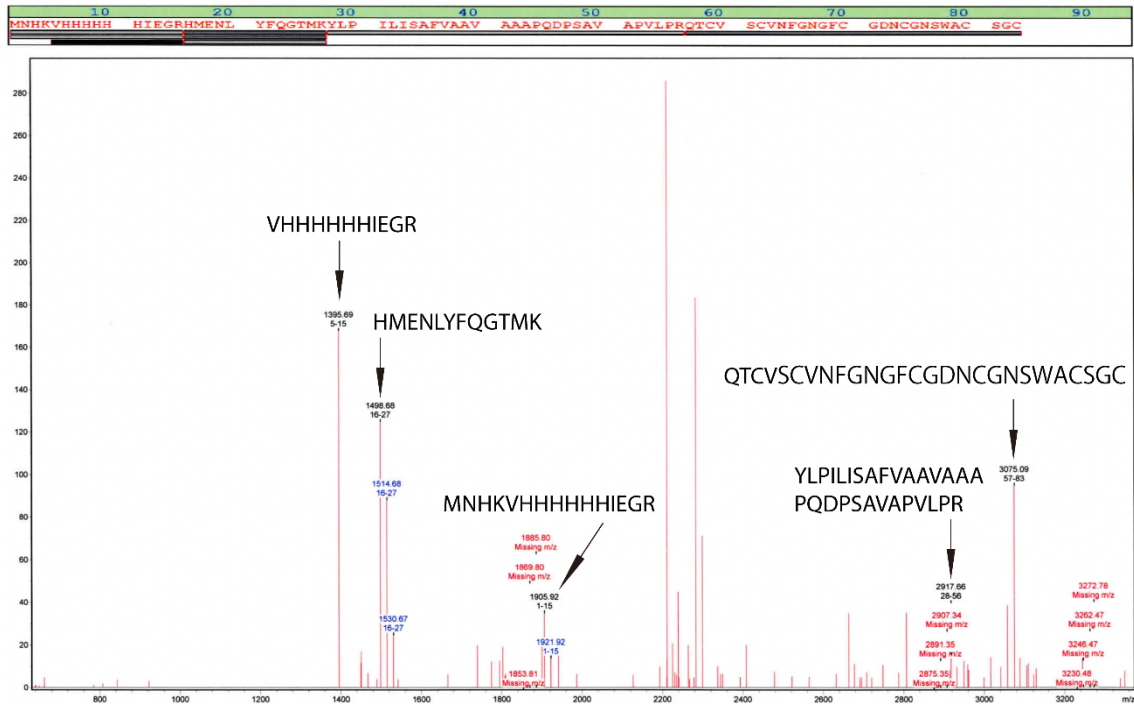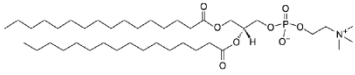
Figure S2. MALDI FT-ICR mass spectrometry of Cas1. The m/z signals in good agreement with the calculated mass are marked by the corresponding amino acid sequences. **Related to Figure S1 and Table S1**.

1. Phospholipids (Plant)

  (a) 16:0 PC (DPPC), MW: 733.562 g/mol, Tm: 41°C, neutral charge
     (1,2-dipalmitoyl-sn-glycero-3-phosphocholine)
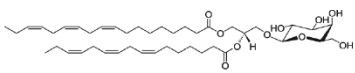
  (b) 16:0 PA (DPPA), MW: 670.455 g/mol, Tm: 65°C, negative charge
     (1,2-dipalmitoyl-sn-glycero-3-phosphate (sodium salt))
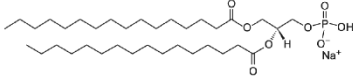
2. Glycerolipids (Plant)

  (c) MGDG, MW: 774.530 g/mol, Tm: unknown, negative charge
     (Monogalactosyldiacylglycerol (Plant))

  (d) DGDG, MW: 926.767 g/mol, Tm: unknown, negative charge
     (Digalactosyldiacylglycerol (Plant))
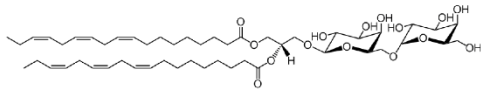
3. Sterols (Plant)

  (e) Stigmasterol, MW: 412.371 g/mol, Tm: 165 - 167°C, neutral charge
     (Stigmasta-5,22-dien-3-ol)
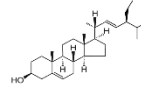
  (f) Sitosterol, MW: 414.386 g/mol, Tm: unknown, neutral charge
     (22,23-dihydrostigmasterol)
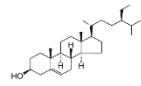
4. Betaine lipids (Plant)

  (g) DGTS-d9, MW: 720.658 g/mol, Tm: unknown, neutral charge
     (1,2-dipalmitoyl-sn-glycero-3-O-4'-[N,N,N-trimethyl(d9)]-betaine)
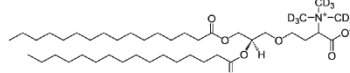
  (h) DGTS, MW: 711.601 g/mol, Tm: unknown, neutral charge
     (1,2-dipalmitoyl-sn-glycero-3-O-4'-(N,N,N-trimethyl)-betaine)
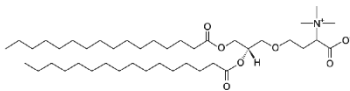
Figure S3. Structures and physical properties of different lipids available in plants. Tm: melting temperature. Data were obtained from Avanti Polar Lipids (Alabama, USA). **Related to Figures 1, 2, and 3**.
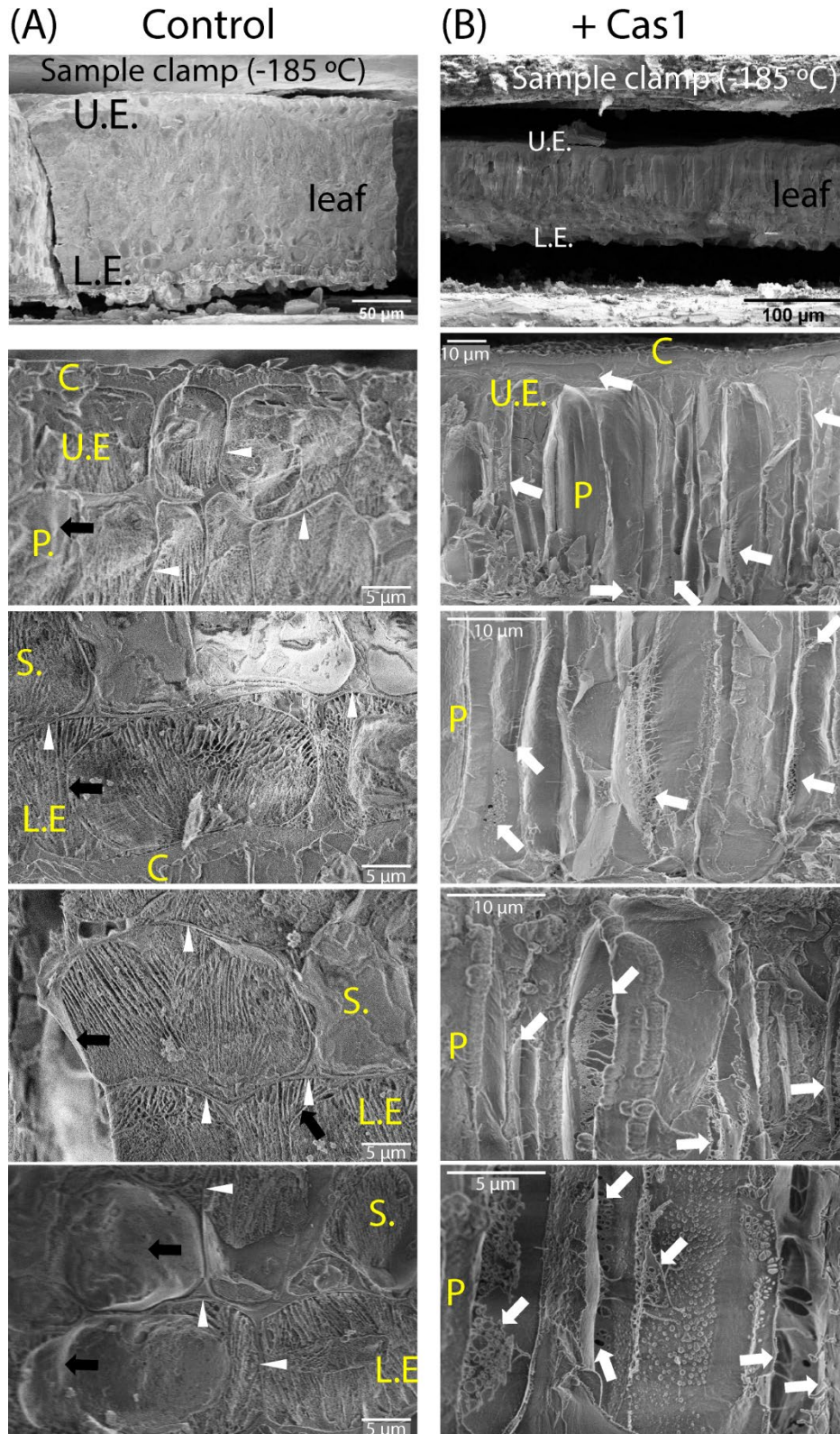
Figure S4. Cryo-SEM images of cellular and tissue structures of control and lesion spots in rubber leaves (rubber clone RRIV 4) caused by Cas1. Black and white arrows denote healthy and unhealthy cytoplasmic membranes, respectively. White arrowheads denote the cell wall. C: cuticle; U.E.: upper epidermis; L.E.: lower epidermis; P.: palisade; S.: spongy. **Related to**

Figures 4 and 5.

Table S1. Peptides predicted for and detected (red characters) by MALDI FT-ICR mass spectrometry. **Related to Figure S2**.

Peptide ID	Amino acid number	Predicted Mass	Number of uncleaved sites	Sequence and modifications
1	[1 – 4]	529.255	0	MNHK
1	[1 – 4]	545.250	0	MNHK (1 * Oxidation (M))
2	[1 – 15]	1905.926	1	MNHKVHHHHHHIEGR
2	[1 – 15]	1921.921	1	MNHKVHHHHHHIEGR (1 * Oxidation (M))
3	[1 – 27]	3385.590	2	MNHKVHHHHHHIEGR HMENLYFQGTMK
3	[1 – 27]	3401.585	2	MNHKVHHHHHHIEGR HMENLYFQGTMK (1 * Oxidation (M))
3	[1 – 27]	3417.580	2	MNHKVHHHHHHIEGR HMENLYFQGTMK (2 * Oxidation (M))
3	[1 – 27]	3433.575	2	MNHKVHHHHHHIEGR HMENLYFQGTMK (3 * Oxidation (M))
4	[5 – 15]	1395.689	0	VHHHHHHIEGR
5	[5 – 27]	2875.353	1	VHHHHHHIEGRHMENLYFQGTMK
5	[5 – 27]	2891.348	1	VHHHHHHIEGRHMENLYFQGTMK (1 * Oxidation (M))
5	[5 – 27]	2907.343	1	VHHHHHHIEGRHMENLYFQGTMK (2 * Oxidation (M))
7	[16 – 27]	1498.682	0	HMENLYFQGTMK
7	[16 – 27]	1514.677	0	HMENLYFQGTMK (1 * Oxidation (M))
7	[16 – 27]	1530.672	0	HMENLYFQGTMK (2 * Oxidation (M))
8	[16 – 56]	4397.319	1	HMENLYFQGTMKYLPILISAFVA AVAAAPQDPSAVAPVLPR
8	[16 – 56]	4413.314	1	HMENLYFQGTMKYLPILISAFVA

				AVAAAPQDPSAVAPVLPR (1 * Oxidation (M))
8	[16 – 56]	4429.309	1	HMENLYFQGTMKYLPILISAFVA AVAAAPQDPSAVAPVLPR (2 * Oxidation (M))
10	[28 – 56]	2917.655	0	YLPILISAFVAAVAAAPQDPSAVA PVLPR
12	[57 – 83]	3075.100	0	QTCVSCVNFGNGFCGDNCGNSW ACSGC (6 * Carbamidomethyl (C))

Table S2. Classification of the susceptibility of different lipids available in plant cytoplasmic membranes to Cas1 and Cas2. Here, we compared the binding and disruption activities of Cas1 and Cas2 to the lipid membranes acquired in HS-AFM and confocal microscopic analyses. The binding and disruption activities of Cas1 and Cas2 to the neutral DPPC lipid membranes were used as the basal indicator for a semiquantitative comparison. ++: strong; +: weak; B: Binding; D: Disruption. **Related to Figures 1,2,3, Table S4, and Movies S1 – S16**.

	DPPC	DPPC/ DPPA	DPPC/ MGDG	DPPC/ DGDG	DPPC/ Stigmasterol	DPPC/ Sitosterol	DPPC/ DGTS-d9	DPPC/ DGTS
+ Cas1	B (+)	B (++)	B (++)	B (++)	B (+)	B (+)	B (+)	B (+)
	D (+)	D (++)	D (++)	D (++)	D (++)	D (+)	D (+)	D (+)
+ Cas2	B (+)	B (++)	B (++)	B (++)	B (++)	B (++)	B (++)	B (++)
	D (+)	D (++)	D (++)	D (++)	D (++)	D (++)	D (+)	D (+)

Table S3. Lipid compositions for making giant liposome vesicles (GVs). **Related to Figure 3**

GVs	DPPC	DPPC/ DPPA	DPPC/ MGDG	DPPC/ DGDG	DPPC/ Stigmasterol	DPPC/ Sitosterol	DPPC/ DGTS-d9	DPPC/ DGTS
DPPC	10 mM	8 mM	7.5 mM	7.5 mM	9 mM	9 mM	7.5 mM	7.5 mM
DPPA		2 mM						
MGDG			2.5 mM					
DGDG				2.5 mM				
Stimasterol					1 mM			
Sitosterol						1 mM		
DGTS-d9							2.5 mM	
DGTS								2.5 mM
18:1 Liss Rhod PE	0.1 mM	0.1 mM	0.1 mM	0.1 mM	0.1 mM	0.1 mM	0.1 mM	0.1 mM
16:0 Biotinyl PE	0.5 mM	0.5 mM	0.5 mM	0.5 mM	0.5 mM	0.5 mM	0.5 mM	0.5 mM

Table S4. Quantification of relative fluorescence areas of GFP-Cas1 and GFP-Cas2 on different GVs. The values are mean ± SD. The two-independent populations *t-test* was used to examine the significant differences, and *p*-values and number of values (N) are shown in parentheses. GFP fluorescence areas on DPPC GVs were used as the controls for comparison with those on other GVs. **Related to Figure 3**.

GVs Samples	Relative fluorescence areas of GFP-Cas1 (mean ± SD) % (*p* value, N)	Relative fluorescence areas of GFP-Cas2 (mean ± SD) % (*p* value, N)
a1,a2 (DPPC)	11.2 ± 6.9 (1.0000, 8)	11.8 ± 6.4 (1.0000, 7)
b1.b2 (PPPC/DPPA)	38.1 ± 12.7 (0.0002, 8)	52.2 ± 6.4 (0.0000001, 7)
c1,c2 (DPPC/MGDG)	22.5 ± 4.6 (0.0048, 7)	33.2 ± 9.5 (0.0006368, 7)
d1,d2 (DPPC/DGDG)	30.7 ± 5.7 (0.00003, 9)	35.9 ± 4.6 (0.0000004, 10)
e1,e2 (DPPC/stigmasterol)	22.7 ± 15.7 (0.0961, 8)	30.6 ± 7.5 (0.0002098, 9)
f1,f2 (DPPC/sitosterol)	19.2 ± 9.9 (0.1130, 8)	30.9 ± 9.3 (0.0004778, 10)
g1,g2 (DPPC/DGTS-d9)	18.6 ± 9.7 (0.1211, 8)	30.0 ± 3.4 (0.0001303, 6)
h1,h2 (DPPC/DGTS)	11.4 ± 10.3 (0.9688, 7)	30.3 ± 10.5 (0.0011800, 11)

Table S5. Information on oligonucleotide sequences of genes encoding Cas1 and Cas2 and amino acid sequences of recombinant Cas1, Cas2, GFP-Cas1, and GFP-Cas2 proteins. We explain amino acid sequences in Cas1 and Cas2; bold letters are full-length Cas1 and Cas2 proteins, in which the signal peptides are underlined letters followed by the putative mature domains. The italic letters indicate a 6xHis-tag followed by TEV protease recognition sites on the N-terminal domain of Cas1 and Cas2 for purifying these recombinant proteins. For GFP-Cas1 and GFP-Cas2, bold letters are a fusion of GFP (underlined and bold letters) with Cas1 or Cas2 (bold letters). The italic letters indicate a 6xHis-tag followed by the amino acid linker. **Related to Figure S1**.

Cas1 GenBank: ABV25895	5'atgaaatatctccctatcctcatctctgcttttgtagcagccgttgctgcagcccc gcaagatccgtctgctgtggcacctgtactccctagacagacttgcgtaagctgtg tcaatttcggcaatgggttttgtggcgataactgtggtaattcttgggcttgttcggga tgttaa3'
Cas2 GenBank: ADC54229	5'atgaaatacctccctatcttcatctctgcttttgtagcagccgttgctgcagttccg cagggtccgtctgctgcggcagcagctattcttcctagacagtcttgcgtatcatgt gtcgatttcggcaacgggttctgtggcgacaactgtggtaattcctgggcttgttcg ggttgttag3'
FWCas1 primer (KpnI) FWGFP-Cas1 primer (in-fusion)	5' GGTACCatgaaatatctccctatcc 3' 5' ACTATACGGTGGATCCatgaaatatctccctatcct 3'
RVCas1 primer (XbaI) RVGFP-Cas1 primer (in-fusion)	5' TCTAGAttaacatcccgaacaagcc 3' 5' ACTATACGGTGGATCCatgaaatatctccctatcct 3'
FWCas2 primer (KpnI) FWGFP-Cas2 primer (in-fusion)	5' GGTACCatgaaatacctccctatct 3' 5' ACTATACGGTGGATCCatgaaatacctccctatct 3'
RVCas2 primer (XbaI) RVGFP-Cas2 primer (in-fusion)	5' TCTAGActaacaacccgaacaagc 3' 5' GCAGGTCGACAAGCTTctaacaacccgaacaag 3'
Cas1, 83 amino acids, 9003.27 Da	*M N H K V H H H H H H I E G R H M E N L Y F Q G T* **M** **<u>K Y L P I L I S A F V A A V A A</u>** **A P Q D P S A V A P V L P R Q T C V S C V N F G N G F C G D N C G N S W A C S G C ***
Cas2, 84 amino acids, 9025.28 Da	*M N H K V H H H H H H I E G R H M E N L Y F Q G T* **M** **<u>K Y L P I F I S A F V A A V A A</u>** **V P Q G P S A A A A A I L P R Q S C V S C V D F G N G F C G D N C G N S W A C S G C ***
GFP-Cas1, 319 amino	*M N H K V H H H H H H I E G R H M E L G T* **<u>M S K G</u>**

acids, 35400.95 KDa	**E E L F T G V V P I L V E L D G** ------- **F G N G F C G D N C G N S W A C S G C ***
GFP-Cas2, 320 amino acids, 35422.07 KDa	*M N H K V H H H H H H I E G R H M E L G T* **M S K G E E L F T G V V P I L V E L D G** -------- **D F G N G F C G D N C G N S W A C S G C ***

Movie S1. Disruption of DPPC membrane lipids caused by Cas1. Briefly, DPPC lipid bilayers were formed on mica by rupturing DPPC liposomes. Then, 0.95 μM Cas1 was added, and HS-AFM imaging was carried out in C-buffer using BL-AC10DS-A2 cantilever deposited with a small Lab-made tip. AFM imaging rate: 2 fps. The movie plays at 30 fps. Bars: 50 nm. **Related to Figures 1a1, S3, and Table S2**.

Movie S2. Disruption of DPPC membrane lipids caused by Cas2. Briefly, DPPC lipid bilayers were formed on mica by rupturing DPPC liposomes. Then, 0.95 μM Cas2 was added, and HS-AFM imaging was carried out in C-buffer using BL-AC10DS-A2 cantilever deposited with a small Lab-made tip. AFM imaging rate: 2 fps. The movie plays at 30 fps. Bars: 50 nm. **Related to Figures 1a2, S3, and Table S2**.

Movie S3. Disruption of DPPC/DPPA membrane lipids caused by Cas1. Briefly, DPPC/DPPA (85/20 wt%) lipid bilayers were formed on mica by rupturing DPPC/DPPA liposomes. Then, 0.95 μM Cas1 was added, and HS-AFM imaging was carried out in C-buffer using BL-AC10DS-A2 cantilever deposited with a small Lab-made tip. AFM imaging rate: 2 fps. The movie plays at 30 fps. Bars: 50 nm. **Related to Figures 1b1, S3, and Table S2**.

Movie S4. Disruption of DPPC/DPPA membrane lipids caused by Cas2. Briefly, DPPC/DPPA (85/20 wt%) lipid bilayers were formed on mica by rupturing DPPC/DPPA liposomes. Then, 0.95 μM Cas2 was added, and HS-AFM imaging was carried out in C-buffer using BL-AC10DS-A2 cantilever deposited with a small Lab-made tip. AFM imaging rate: 2 fps. The movie plays at 30 fps. Bars: 50 nm. **Related to Figures 1b2, S3, and Table S2**.

Movie S5. Disruption of DPPC/MGDG membrane lipids caused by Cas1. Briefly, DPPC/MGDG (80/20 wt%) lipid bilayers were formed on mica by rupturing DPPC/MGDG liposomes. Then, 0.95 μM Cas1 was added, and HS-AFM imaging was carried out in C-buffer using BL-AC10DS-A2 cantilever deposited with a small Lab-made tip. AFM imaging rate: 2 fps. The movie plays at 30 fps. Bars: 50 nm. **Related to Figures 1c1, S3, and Table S2**.

Movie S6. Disruption of DPPC/MGDG membrane lipids caused by Cas2. Briefly, DPPC/MGDG (80/20 wt%) lipid bilayers were formed on mica by rupturing DPPC/MGDG liposomes. Then, 0.95 μM Cas2 was added, and HS-AFM imaging was carried out in C-buffer using BL-AC10DS-A2 cantilever deposited with a small Lab-made tip. AFM imaging rate: 2 fps. The movie plays at 30 fps. Bars: 50 nm. **Related to Figures 1c2, S3, and Table S2**.

Movie S7. Disruption of DPPC/DGDG membrane lipids caused by Cas1. Briefly, DPPC/DGDG (60/40 wt%) lipid bilayers were formed on mica by rupturing DPPC/DGDG liposomes. Then, 0.95 μM Cas1 was added, and HS-AFM imaging was carried out in C-buffer using BL-AC10DS-A2 cantilever deposited with a small Lab-made tip. AFM imaging rate: 2 fps. The movie plays at 30 fps. Bars: 50 nm. **Related to Figures 1d1, S3, and Table S2**.

Movie S8. Disruption of DPPC/DGDG membrane lipids caused by Cas2. Briefly, DPPC/DGDG (60/40 wt%) lipid bilayers were formed on mica by rupturing DPPC/DGDG liposomes. Then, 0.95 μM Cas2 was added, and HS-AFM imaging was carried out in C-buffer

using BL-AC10DS-A2 cantilever deposited with a small Lab-made tip. AFM imaging rate: 2 fps. The movie plays at 30 fps. Bars: 50 nm. **Related to Figures 1d2, S3, and Table S2**.

Movie S9. Disruption of DPPC/stigmasterol membrane lipids caused by Cas1. Briefly, DPPC/stigmasterol (80/20 wt%) lipid bilayers were formed on mica by rupturing DPPC/stigmasterol liposomes. Then, 0.95 μM Cas1 was added, and HS-AFM imaging was carried out in C-buffer using BL-AC10DS-A2 cantilever deposited with a small Lab-made tip. AFM imaging rate: 2 fps. The movie plays at 30 fps. Bars: 50 nm. **Related to Figures 1e1, S3, and Table S2**.

Movie S10. Disruption of DPPC/stigmasterol membrane lipids caused by Cas2. Briefly, DPPC/stigmasterol (80/20 wt%) lipid bilayers were formed on mica by rupturing DPPC/stigmasterol liposomes. Then, 0.95 μM Cas2 was added, and HS-AFM imaging was carried out in C-buffer using BL-AC10DS-A2 cantilever deposited with a small Lab-made tip. AFM imaging rate: 2 fps. The movie plays at 30 fps. Bars: 50 nm. **Related to Figures 1e2, S3, and Table S2**.

Movie S11. Disruption of DPPC/sitosterol membrane lipids caused by Cas1. Briefly, DPPC/sitosterol (80/20 wt%) lipid bilayers were formed on mica by rupturing DPPC/Sitosterol liposomes. Then, 0.95 μM Cas1 was added, and HS-AFM imaging was carried out in C-buffer using BL-AC10DS-A2 cantilever deposited with a small Lab-made tip. AFM imaging rate: 2 fps. The movie plays at 30 fps. Bars: 50 nm. **Related to Figures 1f1, S3, and Table S2**.

Movie S12. Disruption of DPPC/sitosterol membrane lipids caused by Cas2. Briefly, DPPC/sitosterol (80/20 wt%) lipid bilayers were formed on mica by rupturing DPPC/Sitosterol liposomes. Then, 0.95 μM Cas2 was added, and HS-AFM imaging was carried out in C-buffer using BL-AC10DS-A2 cantilever deposited with a small Lab-made tip. AFM imaging rate: 2 fps. The movie plays at 30 fps. Bars: 50 nm. **Related to Figures 1f2, S3, and Table S2**.

Movie S13. Disruption of DPPC/DGTS-d9 membrane lipids caused by Cas1. Briefly, DPPC/DGTS-d9 (80/20 wt%) lipid bilayers were formed on mica by rupturing DPPC/DGTS-d9 liposomes. Then, 0.95 μM Cas1 was added, and HS-AFM imaging was carried out in C-buffer using BL-AC10DS-A2 cantilever deposited with a small Lab-made tip. AFM imaging rate: 2 fps. The movie plays at 30 fps. Bars: 50 nm. **Related to Figures 1g1, S3, and Table S2**.

Movie S14. Disruption of DPPC/DGTS-d9 membrane lipids caused by Cas2. Briefly, DPPC/DGTS-d9 (80/20 wt%) lipid bilayers were formed on mica by rupturing DPPC/DGTS-d9 liposomes. Then, 0.95 μM Cas2 was added, and HS-AFM imaging was carried out in C-buffer using BL-AC10DS-A2 cantilever deposited with a small Lab-made tip. AFM imaging rate: 2 fps. The movie plays at 30 fps. Bars: 50 nm. **Related to Figures 1g2, S3, and Table S2**.

Movie S15. Disruption of DPPC/DGTS membrane lipids caused by Cas1. Briefly, DPPC/DGTS (80/20 wt%) lipid bilayers were formed on mica by rupturing DPPC/DGTS liposomes. Then, 0.95 μM Cas1 was added, and HS-AFM imaging was carried out in C-buffer using BL-AC10DS-A2 cantilever deposited with a small Lab-made tip. AFM imaging rate: 2

fps. The movie plays at 30 fps. Bars: 50 nm. **Related to Figures 1h1, S3, and Table S2**.

Movie S16. Disruption of DPPC/DGTS membrane lipids caused by Cas2. Briefly, DPPC/DGTS (80/20 wt%) lipid bilayers were formed on mica by rupturing DPPC/DGTS liposomes. Then, 0.95 μM Cas2 was added, and HS-AFM imaging was carried out in C-buffer using BL-AC10DS-A2 cantilever deposited with a small Lab-made tip. AFM imaging rate: 2 fps. The movie plays at 30 fps. Bars: 50 nm. **Related to Figures 1h2, S3, and Table S2**.

References

(1)   Ribeiro, S.; Tran, D. M.; Déon, M.; Clément-Demange, A.; Garcia, D.; Soumahoro, M.; Masson, A.; Pujade-Renaud, V. Gene Deletion of *Corynespora cassiicola* Cassiicolin Cas1 Suppresses Virulence in the Rubber Tree. *Fungal Genet. Biol.* **2019**, *129*, 101–114. https://doi.org/10.1016/j.fgb.2019.05.004.

(2)   Shrestha, S. K.; Lamour, K.; Young-Kelly, H. Genome Sequences and SNP Analyses of *Corynespora cassiicola* from Cotton and Soybean in the Southeastern United States Reveal Limited Diversity. *PLoS One* **2017**, *12* (9), 6–14. https://doi.org/10.1371/journal.pone.0184908.

(3)   Sumabat, L. G.; Kemerait, R. C.; Brewer, M. T. Phylogenetic Diversity and Host Specialization of *Corynespora cassiicola* Responsible for Emerging Target Spot Disease of Cotton and Other Crops in the Southeastern United States. *Phytopathology* **2018**, *108* (7), 892–901. https://doi.org/10.1094/PHYTO-12-17-0407-R.

(4)   Dixon, L. J.; Schlub, R. L.; Pernezny, K.; Datnoff, L. E. Host Specialization and Phylogenetic Diversity of *Corynespora cassiicola*. *Phytopathology* **2009**, *99* (9), 1015–1027. https://doi.org/10.1094/PHYTO-99-9-1015.

(5)   de Lamotte, F.; Duviau, M. P.; Sanier, C.; Thai, R.; Poncet, J.; Bieysse, D.; Breton, F.; Pujade-Renaud, V. Purification and Characterization of Cassiicolin, the Toxin Produced by *Corynespora cassiicola*, Causal Agent of the Leaf Fall Disease of Rubber Tree. *J. Chromatogr. B Anal. Technol. Biomed. Life Sci.* **2007**, *849* (1–2), 357–362. https://doi.org/10.1016/j.jchromb.2006.10.051.

(6)   Barthe, P.; Pujade-Renaud, V.; Breton, F.; Gargani, D.; Thai, R.; Roumestand, C.; de Lamotte, F. Structural Analysis of Cassiicolin, a Host-Selective Protein Toxin from *Corynespora cassiicola*. *J. Mol. Biol.* **2007**, *367* (1), 89–101. https://doi.org/10.1016/j.jmb.2006.11.086.

(7)   Déon, M.; Fumanal, B.; Gimenez, S.; Bieysse, D.; Oliveira, R. R.; Shuib, S. S.; Breton, F.; Sunderasan, E.; Vida, J. B.; Seguin, M.; Leroy, T.; Roeckel-Drevet, P.; Pujade-Renaud, V. Diversity of the Cassiicolin Gene in *Corynespora cassiicola* and Relation with the Pathogenicity in *Hevea brasiliensis*. *Fungal Biol.* **2014**, *118* (1), 32–47. https://doi.org/10.1016/j.funbio.2013.10.011.

(8)   Wu, J.; Xie, X.; Shi, Y.; Chai, A.; Wang, Q.; Li, B. Variation of Cassiicolin Genes among Chinese Isolates of *Corynespora cassiicola*. *J. Microbiol.* **2018**, *56* (9), 634–647. https://doi.org/10.1007/s12275-018-7497-5.

(9)   Déon, M.; Bourré, Y.; Gimenez, S.; Berger, A.; Bieysse, D.; De Lamotte, F.; Poncet, J.; Roussel, V.; Bonnot, F.; Oliver, G.; Franchel, J.; Seguin, M.; Leroy, T.; Roeckel-Drevet, P.; Pujade-Renaud, V. Characterization of a Cassiicolin-Encoding Gene from *Corynespora cassiicola*, Pathogen of Rubber Tree (*Hevea brasiliensis*). *Plant Sci.* **2012**, *185–186*, 227–237. https://doi.org/10.1016/j.plantsci.2011.10.017.

(10) Lopez, D.; Ribeiro, S.; Label, P.; Fumanal, B.; Venisse, J. S.; Kohler, A.; de Oliveira, R. R.; Labutti, K.; Lipzen, A.; Lail, K.; Bauer, D.; Ohm, R. A.; Barry, K. W.; Spatafora, J.; Grigoriev, I. V.; Martin, F. M.; Pujade-Renaud, V. Genome-Wide Analysis of *Corynespora cassiicola* Leaf Fall Disease Putative Effectors. *Front. Microbiol.* **2018**, *9*, 1–21. https://doi.org/10.3389/fmicb.2018.00276.

(11) Hieu, N. D.; Nghia, N. A.; Uyen, N. T. K.; Chau, N. N. B.; Quoc, N. B. Genetic Diversity Analysis of Corynespora Cassiicola Isolates on the Rubber Tree (*Hevea brasiliensis*) in Vietnam Using Ribosomal DNA Internal Transcribed Spacer (RDNA-ITS) Sequences and Sequence-Related Amplified Polymorphism (SRAP). *J. Rubber Res.* **2020**, *23* (3), 173–185. https://doi.org/10.1007/s42464-020-00047-7.

(12) Nghia, N. A.; Kadir, J.; Sunderasan, E.; Puad Abdullah, M.; Malik, A.; Napis, S. Morphological and Inter Simple Sequence Repeat (ISSR) Markers Analyses of *Corynespora cassiicola* Isolates from Rubber Plantations in Malaysia. *Mycopathologia* **2008**, *166* (4), 189–201. https://doi.org/10.1007/s11046-008-9138-8.

(13) Nguyen, H. D.; Nguyen, N. A.; Vu, C. T. Q.; Phan, D. A. Genetic Diversity and Pathogenicity of *Corynespora cassiicola* Isolates from Rubber Trees and Other Hosts in Vietnam. *J. Rubber Res.* **2014**, *17* (3), 187–203.

(14) Tran, D. M.; Clément-Demange, A.; Déon, M.; Garcia, D.; Le Guen, V.; Clément-Vidal, A.; Soumahoro, M.; Masson, A.; Label, P.; Le, M. T.; Pujade-Renaud, V. Genetic Determinism of Sensitivity to *Corynespora cassiicola* Exudates in Rubber Tree(*Hevea brasiliensis*). *PLoS One* **2016**, *11* (10), 1–25. https://doi.org/10.1371/journal.pone.0162807.

(15) Déon, M.; Scomparin, A.; Tixier, A.; Mattos, C. R. R.; Leroy, T.; Seguin, M.; Roeckel-Drevet, P.; Pujade-Renaud, V. First Characterization of Endophytic *Corynespora cassiicola* Isolates with Variant Cassiicolin Genes Recovered from Rubber Trees in Brazil. *Fungal Diversity*. 2012, pp 87–99. https://doi.org/10.1007/s13225-012-0169-6.

(16) Park, P.; Fukutomi, M.; Akai, S.; Nishimura, S. Effect of the Host-Specific Toxin from *Alternaria kikuchiana* on the Ultrastructure of Plasma Membranes of Cells in Leaves of Japanese Pear. *Physiol. Plant Pathol.* **1976**, *9* (2), 167–174. https://doi.org/10.1016/0048-4059(76)90036-9.

(17) Riley, R. T.; Wang, E.; Schroeder, J. J.; Smith, E. R.; Plattner, R. D.; Abbas, N.; Yoo, H. S.; Merrill, A. H. Evidence for Disruption of Sphingolipid Metabolism as a Contributing Factor in the Toxicity and Carcinogenicity of Fumonisins. *Nat. Toxins* **1996**, *4* (1), 3–15. https://doi.org/10.1002/19960401NT2.

(18) Meena, M.; Samal, S. Alternaria Host-Specific (HSTs) Toxins: An Overview of Chemical Characterization, Target Sites, Regulation and Their Toxic Effects. *Toxicol. Reports* **2019**, *6* (July), 745–758. https://doi.org/10.1016/j.toxrep.2019.06.021.

(19) Tsuge, T.; Harimoto, Y.; Akimitsu, K.; Ohtani, K.; Kodama, M.; Akagi, Y.; Egusa, M.;

Yamamoto, M.; Otani, H. Host-Selective Toxins Produced by the Plant Pathogenic Fungus *Alternaria alternata*. *FEMS Microbiol. Rev.* **2013**, *37* (1), 44–66. https://doi.org/10.1111/j.1574-6976.2012.00350.x.

(20) Mackender, R. O.; Leech, R. M. The Galactolipid, Phospholipid, and Fatty Acid Composition of the Chloroplast Envelope Membranes of *Vicia faba . l.* . *Plant Physiol.* **1974**, *53* (3), 496–502. https://doi.org/10.1104/pp.53.3.496.

(21) Poincelot, R. P. Lipid and Fatty Acid Composition of Chloroplast Envelope Membranes from Species with Differing Net Photosynthesis. *Plant Physiol.* **1976**, *58* (4), 595–598. https://doi.org/10.1104/pp.58.4.595.

(22) Dörmann, P.; Benning, C. Galactolipids Rule in Seed Plants. *Trends Plant Sci.* **2002**, *7* (3), 112–118. https://doi.org/10.1016/S1360-1385(01)02216-6.

(23) Liengprayoon, S.; Sriroth, K.; Dubreucq, E.; Vaysse, L. Glycolipid Composition of *Hevea brasiliensis* Latex. *Phytochemistry* **2011**, *72* (14–15), 1902–1913. https://doi.org/10.1016/j.phytochem.2011.04.023.

(24) Bae, S. W.; Jung, S.; Choi, S. C.; Kim, M. Y.; Ryu, S. B. Lipid Composition of Latex and Rubber Particlesin *Hevea brasiliensis* and *Taraxacum kok-saghyz*. *molecules* **2020**, *25* (5110), 1–13. https://doi.org/10.3390/molecules25215110.

(25) Dufourc, E. J. Sterols and Membrane Dynamics. *J. Chem. Biol.* **2008**, *1* (1–4), 63–77. https://doi.org/10.1007/s12154-008-0010-6.

(26) Dufourc, E. J. The Role of Phytosterols in Plant Adaptation to Temperature. *Plant Signal. Behav.* **2008**, *3* (2), 133–134. https://doi.org/10.4161/psb.3.2.5051.

(27) Hartmann, M. A. Plant Sterols and the Membrane Environment. *Trends Plant Sci.* **1998**, *3* (5), 170–175. https://doi.org/10.1016/S1360-1385(98)01233-3.

(28) Murakami, H.; Nobusawa, T.; Hori, K.; Shimojima, M.; Ohta, H. Betaine Lipid Is Crucial for Adapting to Low Temperature and Phosphate Deficiency in *Nannochloropsis*. *Plant Physiol.* **2018**, *177* (1), 181–193. https://doi.org/10.1104/pp.17.01573.

(29) Thatcher, L. F.; Anderson, J. P.; Singh, K. B. Plant Defence Responses: What Have We Learnt From *Arabidopsis*? *Funct. Plant Biol.* **2005**, *32* (1), 1–19. https://doi.org/10.1071/FP04135.

(30) Roy, C. B.; Liu, H.; Rajamani, A.; Saha, T. Transcriptome Profiling Reveals Genetic Basis of Disease Resistance against *Corynespora cassiicola* in Rubber Tree (*Hevea brasiliensis*). *Curr. Plant Biol.* **2019**, *17*, 2–16. https://doi.org/10.1016/j.cpb.2019.02.002.

(31) Ando, T.; Uchihashi, T.; Fukuma, T. High-Speed Atomic Force Microscopy for Nano-Visualization of Dynamic Biomolecular Processes. *Prog. Surf. Sci.* **2008**, *83* (7–9), 337–437. https://doi.org/10.1016/j.progsurf.2008.09.001.

(32) Ando, T.; Uchihashi, T.; Kodera, N.; Yamamoto, D.; Taniguchi, M.; Miyagi, A.; Yamashita, H. High-Speed Atomic Force Microscopy for Nano-Visualization of

Biomolecular Processes. *J. Mol. Recognit.* **2007**, *20*, 448–458. https://doi.org/10.1002/9783527626137.ch12.

(33) Uchihashi, T.; Kodera, N.; Ando, T. Guide to Video Recording of Structure Dynamics and Dynamic Processes of Proteins by High-Speed Atomic Force Microscopy. *Nat. Protoc.* **2012**, *7* (6), 1193–1206. https://doi.org/10.1038/nprot.2012.047.

(34) Ando, T. High-Speed Atomic Force Microscopy Coming of Age. *Nanotechnology* **2012**, *23* (6), 1–27. https://doi.org/10.1088/0957-4484/23/6/062001.

(35) Ando, T.; Uchihashi, T.; Kodera, N. High-Speed AFM and Applications to Biomolecular Systems. *Annu. Rev. Biophys.* **2013**, *42* (1), 393–414. https://doi.org/10.1146/annurev-biophys-083012-130324.

(36) Kodera, N.; Yamamoto, D.; Ishikawa, R.; Ando, T. Video Imaging of Walking Myosin V by High-Speed Atomic Force Microscopy. *Nature* **2010**, *468* (7320), 72–76. https://doi.org/10.1038/nature09450.

(37) Uchihashi, T.; Iino, R.; Ando, T.; Noji, H. High-Speed Atomic Force Microscopy Reveals Rotary Catalysis of Rotorless F1-ATPase. *Science* **2011**, *333*, 755–758. https://doi.org/https://doi.org/10.1126/science.1205510.

(38) Ngo, K. X.; Kodera, N.; Katayama, E.; Ando, T.; Uyeda, T. Q. Cofilin-Induced Unidirectional Cooperative Conformational Changes in Actin Filaments Revealed by High-Speed Atomic Force Microscopy. *Elife* **2015**, *4*, e04806. https://doi.org/10.7554/eLife.04806.

(39) Lin, Y. C.; Chipot, C.; Scheuring, S. Annexin-V Stabilizes Membrane Defects by Inducing Lipid Phase Transition. *Nat. Commun.* **2020**, *11* (1), 1–13. https://doi.org/10.1038/s41467-019-14045-w.

(40) Shibata, M.; Nishimasu, H.; Kodera, N.; Hirano, S.; Ando, T.; Uchihashi, T.; Nureki, O. Real-Space and Real-Time Dynamics of CRISPR-Cas9 Visualized by High-Speed Atomic Force Microscopy. *Nat. Commun.* **2017**, *8* (1), 1–9. https://doi.org/10.1038/s41467-017-01466-8.

(41) Kodera, N.; Noshiro, D.; Dora, S. K.; Mori, T.; Habchi, J.; Blocquel, D.; Gruet, A.; Dosnon, M.; Salladini, E.; Bignon, C.; Fujioka, Y.; Oda, T.; Noda, N. N.; Sato, M.; Lotti, M.; Mizuguchi, M.; Longhi, S.; Ando, T. Structural and Dynamics Analysis of Intrinsically Disordered Proteins by High-Speed Atomic Force Microscopy. *Nat. Nanotechnol.* **2020**. https://doi.org/10.1038/s41565-020-00798-9.

(42) Heath, G. R.; Scheuring, S. Advances in High-Speed Atomic Force Microscopy (HS-AFM) Reveal Dynamics of Transmembrane Channels and Transporters. *Curr. Opin. Struct. Biol.* **2019**, *57*, 93–102. https://doi.org/10.1016/j.sbi.2019.02.008.

(43) Karner, A.; Nimmervoll, B.; Plochberger, B.; Klotzsch, E.; Horner, A.; Knyazev, D. G.; Kuttner, R.; Winkler, K.; Winter, L.; Siligan, C.; Ollinger, N.; Pohl, P.; Preiner, J. Tuning Membrane Protein Mobility by Confinement into Nanodomains. *Nat. Nanotechnol.*

2017, *12* (3), 260–266. https://doi.org/10.1038/nnano.2016.236.

(44) Nasrallah, H.; Vial, A.; Nicolas, P.; Soulier, J.; Costa, L.; Godefroy, C.; Bourillot, E.; Lesniewska, E.; Milhiet, P.-E.; Affiliations. Imaging Artificial Membranes Using High-Speed Atomic Force Microscopy. *Methods Mol. Biol.* **2019**, *1886*, 45–59. https://doi.org/10.1007/978-1-4939-8894-5_3.

(45) Ando, T. High-Speed Atomic Force Microscopy and Its Future Prospects. *Biophys. Rev.* **2018**, *10* (2), 285–292. https://doi.org/10.1007/s12551-017-0356-5.

(46) Carvalho, K.; Ramos, L.; Roy, C.; Picart, C. Giant Unilamellar Vesicles Containing Phosphatidylinositol(4,5) Bisphosphate: Characterization and Functionality. *Biophys. J.* **2008**, *95* (9), 4348–4360. https://doi.org/10.1529/biophysj.107.126912.

(47) Drücker, P.; Iacovache, I.; Bachler, S.; Zuber, B.; Babiychuk, E. B.; Dittrich, P. S.; Draeger, A. Membrane Deformation and Layer-by-Layer Peeling of Giant Vesicles Induced by the Pore-Forming Toxin Pneumolysin. *Biomater. Sci.* **2019**, *7* (9), 3693–3705. https://doi.org/10.1039/c9bm00134d.

(48) Osumi, M.; Konomi, M.; Sugawara, T.; Takagi, T.; Baba, M. High-Pressure Freezing Is a Powerful Tool for Visualization of *Schizosaccharomyces pombe* Cells: Ultra-Low Temperature and Low-Voltage Scanning Electron Microscopy and Immunoelectron Microscopy. *J. Electron Microsc. (Tokyo).* **2006**, *55* (2), 75–88. https://doi.org/10.1093/jmicro/dfl014.

(49) Maure, C.; Verdoucq, L.; Luu, D. T.; Santoni, V. Plant Aquaporins: Membrane Channels with Multiple Integrated Functions. *Annu. Rev. Plant Biol.* **2008**, *59*, 595–624. https://doi.org/10.1146/annurev.arplant.59.032607.092734.

(50) Assmann, S. M.; Haubrick, L. L. Transport Proteins of the Plant Plasma Membrane. *Curr. Opin. Cell Biol.* **1996**, *8* (4), 458–467. https://doi.org/10.1016/S0955-0674(96)80021-4.

(51) Kang, J.; Park, J.; Choi, H.; Burla, B.; Kretzschmar, T.; Lee, Y.; Martinoia, E. Plant ABC Transporters. *Arab. B.* **2011**, *9*, e0153. https://doi.org/10.1199/tab.0153.

(52) Slier, D. J.; Goodrich-Tanrikulu, M.; Cornish, K.; Stafford, A. E.; McKeon, T. A. Composition of Rubber Particles of *Hevea brasiliensis*, *Parthenium argentatum*, *Ficus elastica*, and *Euphorbia lactiflua* Indicates Unconventional Surface Structure. *Plant Physiology and Biochemistry*. 1997, pp 881–889.

(53) Takaoka, S.; Kurata, M.; Harimoto, Y.; Hatta, R.; Yamamoto, M.; Akimitsu, K.; Tsuge, T. Complex Regulation of Secondary Metabolism Controlling Pathogenicity in the Phytopathogenic Fungus *Alternaria alternata*. *New Phytol.* **2014**, *202* (4), 1297–1309. https://doi.org/10.1111/nph.12754.

(54) Petrov, V.; Qureshi, M. K.; Hille, J.; Gechev, T. Occurrence, Biochemistry and Biological Effects of Host-Selective Plant Mycotoxins. *Food Chem. Toxicol.* **2018**, *112*, 251–264. https://doi.org/10.1016/j.fct.2017.12.047.

(55)   Angelova, M. I.; Dimitrov, D. S. Liposome Electroformation. *Faraday Discuss. Chem. Soc.* **1986**, *81*, 303–311.

(56)   Dimitrov, D. S.; Angelova, M. I. Lipid Swelling and Liposome Formation Mediated by Electric Fields. *Bioelectrochemistry Bioenerg.* **1988**, *19* (2), 323–336. https://doi.org/10.1016/0302-4598(88)80013-8.

(57)   Angelova, M.; Dimitrov, D. S. A Mechanism of Liposome Electroformation. *Trends Colloid Interface Sci. II* **2007**, *76*, 59–67. https://doi.org/10.1007/bfb0114171.

(58)   Hellman, U.; Wernstedt, C.; Gonez, J.; Heldin, C.-H. Improvement of an "In-Gel" Digestion Procedure for the Micropreparation of Internal Protein Fragments for Amino Acid Sequencing. *Anal. Biochem.* **1995**, *224*, 451–455.

(59)   Kawakita, Y.; Kinoshita, M.; Furukawa, Y.; Tulum, I.; Tahara, Y. O.; Katayama, E.; Namba, K.; Miyata, M. Structural Study of MPN387, an Essential Protein for Gliding Motility of a Human-Pathogenic Bacterium, *Mycoplasma pneumoniae. J. Bacteriol.* **2016**, *198* (17), 2352–2359. https://doi.org/10.1128/JB.00160-16.